Draft version December 9, 2009
Preprint typeset using LaTeX style emulateapj v. 10/09/06

NEW LIMITS ON AN INTERMEDIATE MASS BLACK HOLE IN OMEGA CENTAURI: II. DYNAMICAL MODELS*

Roeland P. van der Marel & Jay Anderson
Space Telescope Science Institute, 3700 San Martin Drive, Baltimore, MD 21218

(Received May 4, 2009; Accepted Dec 8, 2009)
Draft version December 9, 2009

ABSTRACT

We present a detailed dynamical analysis of the projected density and kinematical data available for the globular cluster ω Centauri. We solve the spherical anisotropic Jeans equation for a given density profile to predict the projected profiles of the RMS velocity $\bar{\sigma}(R)$, in each of the three orthogonal coordinate directions (line of sight, proper motion radial, and proper motion tangential). The models allow for the presence of a central dark mass, such as a possible intermediate-mass black hole (IMBH). We fit the models to new HST star count and proper motion data near the cluster center presented in Paper I, combined with existing ground-based measurements at larger radii. The projected density profile is consistent with being flat near the center, with an upper limit $\gamma \lesssim 0.07$ on the central logarithmic slope. The RMS proper motion profile is also consistent with being flat near the center. The velocity anisotropy profile, distance, and stellar mass-to-light ratio are all tightly constrained by the data, and found to be in good agreement with previous determinations by van de Ven et al. To fit the kinematics we consider anisotropic models with either a flat core ($\gamma = 0$) or a shallow cusp ($\gamma = 0.05$). Core models provide a good fit to the data with $M_{\rm BH} = 0$; cusp models require a dark mass. If the dark mass in cusp models is an intermediate-mass black hole (IMBH), then $M_{\rm BH} = (8.7 \pm 2.9) \times 10^3\,M_\odot$; if it is a dark cluster, then its extent must be $\lesssim 0.16$ pc. Isotropic models do not fit the observed proper motion anisotropy and yield spuriously high values for any central dark mass. These models do provide a good fit to the Gauss-Hermite moments of the observed proper motion distributions ($h_4 = -0.023 \pm 0.004$, $h_6 = 0.001 \pm 0.004$). There are no unusually fast-moving stars observed in the wings of the proper motion distribution, but we show that this does not strongly constrain the mass of any possible IMBH. The overall end-result of the modeling is an upper limit to the mass of any possible IMBH in ω Centauri: $M_{\rm BH} \lesssim 1.2 \times 10^4\,M_\odot$ at $\sim 1\sigma$ confidence (or $\lesssim 1.8 \times 10^4\,M_\odot$ at $\sim 3\sigma$ confidence). The 1σ limit corresponds to $M_{\rm BH}/M_{\rm tot} \lesssim 0.43\%$. We combine this with results for other clusters and discuss the implications for globular cluster IMBH demographics. Tighter limits will be needed to rule out or establish whether globular clusters follow the same black hole demographics correlations as galaxies. The arguments put forward by Noyola et al. to suspect an IMBH in ω Centauri are not confirmed by our study; the value of $M_{\rm BH}$ they suggested is firmly ruled out.

Subject headings: globular clusters: individual (ω Centauri) — stars: kinematics.

1. INTRODUCTION

Intermediate-mass black holes (IMBHs) are of interest in a variety of astrophysical contexts (see, e.g., the reviews by van der Marel 2004; Miller & Colbert 2004). Especially the possible presence of IMBHs in the centers of globular clusters has intrigued astronomers for decades (e.g., Bahcall & Wolf 1976). This subject area underwent a considerable resurgence in recent years due to a combination of two advances. First, theoretical modeling suggested plausible formation scenarios for IMBHs in the centers of globular clusters from realistic initial conditions (Portegies Zwart & McMillan 2002). Second, the quality of observational data sets, especially those obtained with the Hubble Space Telescope (HST), advanced to the point where it is possible to measure velocity dispersions at a spatial resolution comparable to the sphere of influence size for plausible IMBH masses. This led to the identification of three globular clusters with candidate IMBHs, namely M15, G1, and ω Centauri.

Gerssen et al. (2002) used line-of-sight velocity data for individual stars in the core-collapsed cluster M15 (NGC 7078) to argue for the presence of $\sim 3000\,M_\odot$ in dark material near the center, possibly in the form of an IMBH. Dull et al. (1997) and Baumgardt et al. (2003a) showed that this could be a plausible result of mass-segregation, and need not be an IMBH. Moreover, Baumgardt et al. (2005) argued that the observed steep brightness profile of M15, typical of the class of core-collapsed clusters, is in fact not consistent with expectation for a relaxed distribution of stars around an IMBH. Ho, Terashima, & Okajima (2003) and Bash et al. (2008) failed to detect X-ray or radio emission coincident with the cluster center. This is not necessarily inconsistent with an IMBH, since the accretion rate and/or the accretion efficiency are likely to be low. Nonetheless, M15 does not appear to be as strong an IMBH candidate as once thought.

Gebhardt et al. (2002, 2005) used the velocity dispersion measured from integrated light near the center of the M31 cluster G1 to argue for the presence of a

*BASED ON OBSERVATIONS WITH THE NASA/ESA *HUBBLE SPACE TELESCOPE*, OBTAINED AT THE SPACE TELESCOPE SCIENCE INSTITUTE, WHICH IS OPERATED BY AURA, INC., UNDER NASA CONTRACT NAS 5-26555.

$(1.8 \pm 0.5) \times 10^4\ M_\odot$ dark mass at the cluster center. The relaxation time of G1 is too long to have produced such a concentration of dark mass due to mass segregation. Therefore, this result was taken as evidence of for the presence of an IMBH. Baumgardt et al. (2003b) disagreed with this interpretation, and argued that models with no dark mass (IMBH or otherwise) provided an equally acceptable fit. The crux of this disagreement lies in the extremely small size of the sphere of influence ($GM_{\rm BH}/\sigma^2 \approx 0.03''$) of the putative IMBH, which is less than the spatial resolution of the observations. Phrased differently, the IMBH induces only a small signature in the data. As a result, the interpretation of the data is sensitive to the exact details of the data-model comparison. The statistical significance of the IMBH detection is not high, especially if one takes into account the possibility of "black hole bias" (discussed later in Section 6.3). On the other hand, the possible presence of an IMBH in G1 recently gained further credence with the detection of weak X-ray and radio emission from near the cluster center (Pooley & Rappaport 2006; Kong 2007; Ulvestad, Greene & Ho 2007). The emission properties are consistent with accretion onto an IMBH, but other explanations cannot be ruled out.

Noyola et al. (2008; hereafter NGB08) argued for the presence of an IMBH in the center of the cluster ω Centauri (NGC 5139), which is well known for its many enigmatic properties (e.g., Meylan 2002). The dynamics of this cluster were studied previously by van de Ven et al. (2006; hereafter vdV06) using sophisticated axisymmetric models. However, there was insufficient kinematical data at small radii to meaningfully constrain the possible presence of any dark mass. NGB08 performed integrated-light measurements of the line-of-sight velocity dispersion for two $5 \times 5''$ fields, one on the cluster center that they had determined, and one at $R = 14''$ from that center. They obtained $\sigma_{\rm los} = 23.0 \pm 2.0\,{\rm km\,s^{-1}}$ and $\sigma_{\rm los} = 18.6 \pm 1.6\,{\rm km\,s^{-1}}$ for these fields, respectively. The increase in $\sigma_{\rm los}$ towards the cluster center was interpreted to imply the presence of an IMBH of mass $M_{\rm BH} = 4.0^{+0.75}_{-1.0}\ M_\odot$. They also determined the surface brightness profile of ω Centauri from HST images, and inferred a shallow central cusp of logarithmic slope $\gamma = 0.08 \pm 0.03$. This is consistent with theoretical predictions for the cusp induced by an IMBH (Baumgardt et al. 2005).

Both G1 and ω Centauri are somewhat atypical globular clusters. They are the most massive clusters of their parent galaxies, M31 and the Milky Way, respectively. Both clusters have been suggested to be the stripped nuclei of larger galaxies (e.g., Freeman 1993; Meylan et al. 2001). Indeed, the nuclei of galaxies have very similar structural properties to globular clusters (these nuclei are therefore also referred to as nuclear star clusters; e.g., Walcher et al. 2005). Accretion activity is known to exist in at least some of these nuclei (e.g., Seth et al. 2008). So if G1 and ω Centauri contain IMBHs, then these may simply be the low-mass tail of the distribution of supermassive black holes known to exist in galactic nuclei. As such, they would not necessarily be telling us anything fundamentally new about the formation and evolution of globular clusters in general. Nonetheless, G1 and ω Centauri are probably the best current candidates for globular clusters with IMBHs. Validating the existence of their suggested IMBHs is therefore of fundamental importance.

The (initial) IMBH evidence for M15, G1, and ω Centauri was all based on studies of line-of-sight velocities. Such studies are complicated because they require spectroscopy in regions of high stellar density. Integrated-light measurements work well for a cluster as distant as G1 (Gebhardt et al. 2002, 2005), but the downside is that the sphere of influence in such clusters is poorly resolved. In closer Milky Way clusters, the limited number of stars (especially brighter ones) introduces significant shot noise in integrated-light measurements. For ω Centauri, this required special treatment of the data to counteract this (NGB08). For M15, HST/STIS was used to obtain spectroscopy of individual stars (van der Marel et al. 2002). However, the signal-to-noise requirements for a velocity measurement limit the data set to the brightest stars. In turn, this sets the smallest radius inside which a velocity dispersion can be measured.

A significant improvement in data quality is possible with proper motion measurements. Such studies do not require much observing time and allow measurement even of the more numerous faint stars. Moreover, the ratio of the velocity dispersions in the tangential and radial proper motion directions directly constrains the velocity-dispersion anisotropy of the system. This is important because of the well-known mass-anisotropy degeneracy for stellar systems (Binney & Mamon 1982). To determine accurate proper motions close to the center requires an observing platform with high spatial resolution and long-term stability. The HST provides such a platform. McNamara, Harrison, & Anderson (2003) measured proper motions for M15, which were modeled by van den Bosch et al. (2006) and Chakrabarty (2006). This confirmed the presence of dark mass near the cluster center, but did not shed new light on the issue of whether this is due to mass segregation or an IMBH. McLaughlin et al. (2006) obtained and modeled proper motions for 47 Tuc, and used these to set an upper limit of 1000–1500 $M_\odot$ on the mass of any IMBH in that cluster.

In Anderson & van der Marel (2009; hereafter Paper I) we presented the results of a new observational HST study of ω Centauri. For the central few arcmin of the cluster we determined the projected number density distribution of some 10^6 stars, as well as accurate proper motions of some 10^5 stars. The exact position of the cluster center was determined in three independent ways. First, we determined the center of the number density distribution using various methods, taking care to accurately account for incompleteness. Second, we determined the kinematical center, being the symmetry point of the RMS proper motion velocity field. And third, we determined the center of unresolved light seen in 2MASS data. All determinations agree to within 1–2$''$, yielding a final estimate with an uncertainty of $\sim 1''$.

The NGB08 center position, and hence the position of their central spectroscopic field, is at $R = 12''$ from the center determined in Paper I (and coincidentally, the second off-center spectroscopic field they studied is also at $R = 12''$). The differences between the centers determined in these two studies is likely due to a combination of subtle effects that biased the NGB08 analysis, as discussed in Paper I. As a result of this, the density cusp found by NGB08 was not measured around the ac-

tual cluster center. Also, we showed in Paper I that their use of unresolved light (as opposed to star counts) increased the impact of shot noise. In Paper I we determined the number density profile around the actual center of ω Centauri. It was found to be well matched by a standard King model, even though a shallow cusp may not be ruled out.

In Paper I we also determined the RMS proper motions of stars detected in the same $5'' \times 5''$ fields studied spectroscopically by NGB08. For the canonical distance $D = 4.8$ kpc (vdV06), the results translate to one-dimensional values $\bar{\sigma}_{\rm pm} = 18.9 \pm 1.3\ {\rm km\,s^{-1}}$ and $\bar{\sigma}_{\rm pm} = 19.0 \pm 1.6\ {\rm km\,s^{-1}}$, for their "central" and "off-center" fields respectively. So we did not confirm the NGB08 finding that one of their fields has a higher dispersion. The observation that there is no significant difference in proper motion dispersion between the two fields is consistent with our finding that they are both at the same radius $R = 12''$ from the actual cluster center.

Our results of Paper I did not confirm the arguments put forward by NGB08 to suspect the presence of an IMBH in ω Centauri. However, this does not mean that such an IMBH may not be present after all. The size and quality of our proper motion data set are superb. This provides the opportunity to study the central dynamics of ω Centauri at a level of detail that is unmatched by other clusters. We therefore present here a detailed study of the dynamics of ω Centauri, with the primary goal of exploiting the new data from Paper I to constrain the mass of any possible IMBH. We also include existing ground-based data in our data-model comparisons, to obtain the best possible results.

We restrict our modeling efforts in the present paper to spherical models. This is a simplification, given that ω Centauri is elongated and rotating (in fact, unusually so for a globular cluster). However, both the elongation (Geyer, Nelles, & Hopp 1983) and the rotation rate (vdV06) decrease towards the cluster center. Therefore, the assumption of sphericity is likely to be reasonable in the central region most relevant for constraining an IMBH. We find support for this throughout our paper by showing that spherical models yield an anisotropy profile, distance, and mass-to-light ratio that are in excellent agreement with the values obtained by vdV06. More sophisticated models, such as those of the type described by vdV06, van den Bosch et al. (2006) and Chaname et al. (2008), have the potential to constrain other aspects of the structure of ω Centauri, such as its inclination, rotation properties, and the presence of any kinematic subcomponents. However, spherical models are sufficient to obtain robust constraints on the central mass distribution.

The structure of this paper is as follows. Section 2 discusses the general modeling approach. Section 3 presents the data on star count and surface brightness profiles used for the analysis. Section 4 discusses parameterized fits to these data. Section 5 presents the kinematical data used for the analysis. Section 6 presents the kinematical data-model comparison, with a determination of the best-fitting model parameters. Section 7 discusses how the new IMBH results for ω Centauri fit in with our general understanding of IMBH demographics in globular clusters. Section 8 presents and discusses the conclusions.

2. MODELING APPROACH

2.1. *Mass Density*

Imaging observations of a cluster yield an estimate of $\mu_{{\rm obs},X}(R)$, the radial profile of the surface brightness in a photometric band X, averaged over concentric circles of radius R around the cluster center. This quantity is related to the projected intensity $I_{\rm obs}(R)$ according to

$$\mu_X[{\rm magarcsec^{-2}}] = -2.5 \log I_{\rm obs}[L_\odot {\rm pc^{-2}}] + 21.572 + M_{\odot,{\rm X}}, \quad (1)$$

where $M_{\odot,X}$ is the absolute magnitude of the sun in the given photometric band. Throughout this paper, units in which quantities are expressed are given in square brackets where relevant. In the presence of A_X magnitudes of foreground extinction, the extinction-corrected profile is given by

$$I(R) = 10^{0.4 A_{\rm X}}\ I_{\rm obs}(R). \quad (2)$$

For a spherical cluster, $I(R)$ is the line-of-sight integration over the three-dimensional luminosity density $j(r)$. This integration can be inverted through an Abel transform (e.g., Binney & Tremaine 1987) to yield

$$j(r) = -\frac{1}{\pi} \int_r^\infty \left[\frac{dI}{dR}\right](R) \frac{dR}{\sqrt{R^2 - r^2}}. \quad (3)$$

To express this quantity in units of $L_\odot\ {\rm pc^{-3}}$ one needs to specify the cluster distance D. Sizes in arcsec and pc are related according to

$$R[{\rm pc}] = R[{\rm arcsec}]\ \pi\ D[{\rm kpc}]/648. \quad (4)$$

The mass density of stellar objects and their remnants is

$$\rho(r) = [M/L](r)\ j(r), \quad (5)$$

where $[M/L](r)$ is the average mass-to-light ratio at each radius. Gradients in $[M/L](r)$ can be thought of as arising from two separate ingredients: (i) mass segregation among luminous stars; and (ii) mass segregation of the heavy compact stellar remnants (heavy white dwarfs, neutron stars, and stellar-mass black holes) with respect to the luminous stars. The first ingredient generally causes a shallow gradient in $[M/L](r)$ over the scale of the entire cluster (e.g., Gill et al. 2008). This has little effect on the model predictions in the area surrounding the very center, where we wish to search for the signature of an IMBH. By contrast, the second ingredient can in some clusters yield a strong increase in $[M/L](r)$ near the very center (e.g., Dull et al. 1997; Baumgardt et al. 2003a) that mimics the presence of a dark sub-cluster.

Our modeling approach allows for exploration of models with arbitrary $[M/L](r)$. However, we have found it useful and sufficient in the present context to restrict attention to a parameterized subset. Based on the preceding considerations, we write the mass density as

$$\rho(r) \equiv \tilde{\rho}(r) + \rho_{\rm dark}, \qquad \tilde{\rho}(r) \equiv \Upsilon j(r). \quad (6)$$

Here $\tilde{\rho}(r)$ is the mass density obtained under the assumption of a constant mass-to-light ratio Υ. The excess $\rho_{\rm dark}$ is treated mathematically as a separate component. For

$\rho_{\rm dark}$ we have found it convenient to use the parameterization

$$\rho_{\rm dark} = (3M_{\rm dark}a_{\rm dark}^2/4\pi)/(r^2+a_{\rm dark}^2)^{5/2}, \qquad (7)$$

corresponding to a Plummer density distribution. Here $M_{\rm dark}$ is the total excess mass in dark objects and $a_{\rm dark}$ is the characteristic scale length of their spatial distribution. The quantities Υ, $M_{\rm dark}$ and $a_{\rm dark}$ provide a convenient way for exploring a range of plausible $[M/L](r)$ functions using only three parameters.

By assuming that Υ is independent of r, we neglect mass segregation among the luminous stars. For ω Centauri there are in fact several pieces of evidence that it has not yet undergone complete mass segregation, consistent with its long half-mass relaxation time of $\sim 10^{9.96\pm0.03}$ years (McLaughlin & van der Marel 2005). First, Merritt, Meylan & Mayor (1997) constructed non-parametric dynamical models for ω Centauri. They found that at the large radii sampled by their data, $\rho(r) \propto j(r)$ to within the error bars. Second, vdV06 constructed more general dynamical models for a wider range of data, and they too found that at all radii sampled by their study $[M/L](r)$ is consistent with being constant. Third, Anderson (2002) studied luminosity functions (LFs) at different radii in ω Centauri using data obtained with HST. He found that variations in the LFs are less than would be expected if mass segregation had proceeded to the point of energy equipartition. And fourth, in Paper I we studied the proper motion dispersion of stars along the main sequence. This showed that lower mass stars do move faster, but by a smaller amount than would be expected for energy equipartition.

2.2. *Gravitational Potential*

The total gravitational potential of the system is

$$\Phi_{\rm tot} = \tilde{\Phi}(r) + \Phi_{\rm dark}(r) - GM_{\rm BH}/r, \qquad (8)$$

where G is the gravitational constant and $M_{\rm BH}$ is the mass of any central IMBH. The gravitational potential corresponding to $\tilde{\rho}(r)$ is

$$\tilde{\Phi}(r) = -4\pi G\left[\frac{1}{r}\int_0^r \tilde{\rho}(r')r'^2\,dr' + \int_r^\infty \tilde{\rho}(r')r'\,dr'\right]. \qquad (9)$$

The Plummer potential corresponding to $\rho_{\rm dark}$ is

$$\Phi_{\rm dark}(r) = -GM_{\rm dark}/(r^2+a_{\rm dark}^2)^{1/2}. \qquad (10)$$

The potential $\Phi_{\rm tot}$ could in principle be expanded to also include an extended halo of particulate dark matter, but that is more relevant for galaxies. There is no evidence that star clusters are embedded in dark halos. For the specific case of ω Centauri, vdV06 showed that there is no need for dark matter out to at least two half-light radii.

2.3. *Intrinsic Velocity Moments*

The Jeans equation for hydrostatic equilibrium in a spherical stellar system is (e.g., Binney & Tremaine 1987)

$$\frac{d(\nu\overline{v_r^2})}{dr} + 2\frac{\beta\nu\overline{v_r^2}}{r} = -\nu\frac{d\Phi_{\rm tot}}{dr}, \qquad (11)$$

where $\nu(r)$ is the number density of the stars under consideration. Because of the spherical symmetry, $\overline{v_\theta^2} = \overline{v_\phi^2}$. The function $\beta(r) \equiv 1 - \overline{v_{\rm tan}^2}/\overline{v_r^2}$ measures the anisotropy in the second velocity moments, where $\overline{v_{\rm tan}^2} \equiv \overline{v_\theta^2} = \overline{v_\phi^2}$. Models with $\beta = 0$ are isotropic, models with $\beta < 0$ are tangentially anisotropic and models with $0 < \beta \leq 1$ are radially anisotropic. The models may in principle be rotating if $\overline{v_\phi} \neq 0$. However, for the purposes of the present paper we do not need to address how the second azimuthal velocity moment $\overline{v_\phi^2} \equiv \sigma_\phi^2 + \overline{v_\phi}^2$ splits into separate contributions from random motions and mean streaming.

The measured kinematics in a cluster are generally representative for only a subset of the stars (e.g., stars in that magnitude range for which kinematics can be measured). The number density of this subset is

$$\nu(r) = j(r)f(r)/\lambda(r), \qquad (12)$$

where $\lambda(r)$ is the average luminosity of a star in the subset and $f(r)$ is the fraction of the total light that the subset contributes at each radius. Compact stellar remnants play no role in this equation, since they contribute neither to $\nu(r)$ (their kinematics are not probed) nor to $j(r)$ (they emit negligible amounts of light). However, $f(r)$ and $\lambda(r)$ can vary slowly as a function of radius due to mass segregation among the luminous stars. The quantity $\lambda(r)$ may also be affected by observational selection effects that vary as a function of radius. Nonetheless, variations in $\lambda(r)$ will generally be smaller than those in $f(r)$, as long as kinematics are measured for stars of similar brightness at each radius. Both $f(r)$ and $\lambda(r)$ are only expected to have a shallow gradient over the scale of the entire cluster. These gradients are much smaller than those in $j(r)$, which can vary by orders of magnitude. Moreover, in the present paper we are mostly concerned with the small area surrounding the very center. We therefore assume that

$$f(r)/\lambda(r) = \text{constant}, \qquad (13)$$

which implies that, as before, we neglect mass segregation among the luminous stars.

It follows from the preceding that one can substitute $j(r)$ for $\nu(r)$ in the Jeans equation (11), without actually needing to know the value of the constant in equation (13). The Jeans equation is then a linear, first-order differential equation for $j\overline{v_r^2}$ with solution

$$j\overline{v_r^2}(r) = \int_r^\infty j(r')\Big[\frac{d\Phi_{\rm tot}}{dr}\Big](r')\,\exp\Big[2\int_r^{r'}\frac{\beta(r'')\,dr''}{r''}\Big]\,dr'. \qquad (14)$$

This is a special case of a more general solution for certain classes of axisymmetric systems (Bacon, Simien & Monnet 1983). We consider anisotropy functions of the form

$$\beta(r) = (\beta_\infty r^2 + \beta_0 r_a^2)/(r^2+r_a^2), \qquad (15)$$

where $r_a > 0$ is a characteristic anisotropy radius, $\beta_0 \leq 1$ is the central value of $\beta(r)$, and $\beta_\infty \leq 1$ is the asymptotic value at large radii. If $\beta_0 = \beta_\infty$ then $\beta(r)$ is constant. With this $\beta(r)$, equation (14) reduces to

$$j\overline{v_r^2}\,(r) = \int_r^\infty j(r')\left[\frac{d\Phi_{\rm tot}}{dr}\right](r')\;\times \left[\frac{r'^2+r_a^2}{r^2+r_a^2}\right]^{\beta_\infty}\left[\Big(\frac{r'^2}{r^2}\Big)\Big/\Big(\frac{r'^2+r_a^2}{r^2+r_a^2}\Big)\right]^{\beta_0} dr', \qquad (16)$$

which is always positive.

The integral in equation (16) can be used with the equations given for $j(r)$ and $\Phi_{\rm tot}(r)$ in Sections 2.1 and 2.2 to allow numerical evaluation of $\overline{v_r^2}(r)$. This requires knowledge of the observed surface brightness profile $\mu_{{\rm obs},X}(R)$ and the known extinction A_X. It also requires choices for the scalar model quantities D, Υ, $M_{\rm BH}$, $M_{\rm dark}$, $a_{\rm dark}$, β_0, β_∞ and r_a, which can all be chosen to optimize the fit to the available kinematical data.

2.4. *Projected Velocity Moments*

To calculate quantities that are projected along the line of sight, consider an arbitrary point P in the cluster. We adopt a Cartesian coordinate system (pmr, los, pmt) with three orthogonal axis and its origin at the cluster center C. The pmr-axis (proper motion radial) lies in the plane of the sky and points from the projected position of C to the projected position of P. The los-axis (line of sight) points from the observer to the point C. The pmt-axis (proper motion tangential) lies in the plane of the sky, and is orthogonal to the pmr- and los-axes in a right-handed sense. The cylindrical polar coordinate system associated with (pmr, los, pmt) is (R,ϕ,z) and the spherical polar coordinate system is (r,θ,ϕ), with $\theta\in[-\pi/2,\pi/2]$, and $\theta=\pi/2$ corresponding to the pmt axis. The velocities in the (pmr, los, pmt) system satisfy

$$\begin{aligned} v_{\rm pmr} &= v_r\cos\phi - v_\phi\sin\phi,\\ v_{\rm los} &= v_r\sin\phi + v_\phi\cos\phi,\\ v_{\rm pmt} &= v_\theta. \end{aligned} \tag{17}$$

Since $\overline{v_r v_\phi}=0$ in a spherical system, the second moments are

$$\begin{aligned} \overline{v_{\rm pmr}^2}(r,\phi) &= \overline{v_r^2}(r)[1-\beta(r)\sin^2\phi],\\ \overline{v_{\rm los}^2}(r,\phi) &= \overline{v_r^2}(r)[1-\beta(r)\cos^2\phi],\\ \overline{v_{\rm pmt}^2}(r,\phi) &= \overline{v_r^2}(r)[1-\beta(r)], \end{aligned} \tag{18}$$

where we have used that $\overline{v_\phi^2}=\overline{v_\theta^2}=\overline{v_r^2}[1-\beta(r)]$.

The projected second moments satisfy

$$\begin{aligned} I\langle v_{\rm pmr}^2\rangle(R) &= \int_R^\infty \frac{2rj\overline{v_r^2}(r)[1-\beta(r)+\beta(r)(R/r)^2)]\,dr}{\sqrt{r^2-R^2}},\\ I\langle v_{\rm los}^2\rangle(R) &= \int_R^\infty \frac{2rj\overline{v_r^2}(r)[1-\beta(r)(R/r)^2]\,dr}{\sqrt{r^2-R^2}},\\ I\langle v_{\rm pmt}^2\rangle(R) &= \int_R^\infty \frac{2rj\overline{v_r^2}(r)[1-\beta(r)]\,dr}{\sqrt{r^2-R^2}}. \end{aligned} \tag{19}$$

The derivations of these equations use the facts that $\cos^2\phi=(R/r)^2$ and $d{\rm los}=d\sqrt{r^2-R^2}=r dr/\sqrt{r^2-R^2}$. The factor of two arises from the identical contributions from points with los <0 and los >0. The angle brackets around the squared velocities on the left-hand side indicate the combined effect of averaging over velocity space and density-weighted averaging along the line of sight. Formally speaking, the weighting is with number density if one is modeling discrete measurements, and with luminosity density if one is modeling integrated light measurements. However, in the present paper we are assuming that $\nu(r)\propto j(r)$, so the two cases are equivalent. The integrals in equation (19) can be evaluated numerically once the Jeans equation has been solved.

2.5. *Projected Velocity Distributions*

The normalized projected velocity distributions $\mathcal{L}(v,R)$ at projected radius R are generally different for the los, pmr, and pmt directions. The Jeans equation suffices to calculate the second velocity moments of these distributions. To calculate the distributions themselves it is necessary to know the full phase-space distribution function. This is not generally straightforward (or unique) for anisotropic models. However, for an isotropic model the distribution function depends only on the energy, and it can be uniquely calculated for given $j(r)$ (being proportional to both $\nu(r)$ and $\tilde\rho(r)$ under the present assumptions) and $\Phi_{\rm tot}(r)$, with the help of Eddington's equation (Binney & Tremaine 1987). Because of the isotropy, the distribution $\mathcal{L}_{\rm iso}(v,R)$ is independent of the choice of the velocity direction (los, pmr, or pmt) and satisfies, in analogy with equation (19),

$$I(R)\mathcal{L}_{\rm iso}(v,R) = \int_R^{r_{\rm max}(v)} \frac{2rj(r)\mathcal{L}_{\rm loc}(v,r)\,dr}{\sqrt{r^2-R^2}}. \tag{20}$$

Here $r_{\rm max}(v)$ is defined to satisfy $\Psi(r_{\rm max})\equiv\frac{1}{2}v^2$, with $\Psi\equiv-\Phi_{\rm tot}$. The quantity $\mathcal{L}_{\rm loc}(v,r)$ is the local velocity distribution (before projection along the line of sight) at radius r, which can be written with the help of Eddington's equation as (van der Marel 1994a)

$$j(r)\mathcal{L}_{\rm loc}(v,r) = \frac{1}{\pi\sqrt{2}}\int_0^{\Psi(r)-\frac{1}{2}v^2}\left[\frac{dj}{d\Psi}\right]_{\Psi'}\frac{d\Psi'}{\sqrt{\Psi(r)-\frac{1}{2}v^2-\Psi'}}. \tag{21}$$

The integrals in equations (20) and (21) can be used with the equations given for $j(r)$ and $\Phi_{\rm tot}(r)$ in Sections 2.1 and 2.2 to allow numerical evaluation of $\mathcal{L}_{\rm iso}(v,R)$. The result is a symmetric function of v [i.e., $\mathcal{L}_{\rm iso}(v,R)=\mathcal{L}_{\rm iso}(-v,R)$]. This remains true if the distribution function is given a non-zero odd part in the angular momentum L_z around some axis (corresponding to a rotating model), provided that $\mathcal{L}_{\rm iso}(v,R)$ is then interpreted as the distribution averaged over a circle of radius R.

2.6. *Observed quantities*

Equations (19) and (20) define velocity moments and velocity distributions at a fixed position on the projected plane of the sky. However, to determine these quantities observationally it is necessary to gather observations over a finite area. In integrated-light measurements this happens naturally through the use of, e.g., apertures, fibers, or pixels along a long slit of finite width. In discrete measurements of individual stars this happens by binning the data during analysis. In either case, the corresponding model predictions are obtained as a density-weighted integral over the corresponding area in the projected (x,y) plane of the sky. For example, the second line-of-sight velocity moment over an aperture is

$$\langle v_{\rm los}^2\rangle_{\rm ap} = \int_{\rm ap} I\langle v_{\rm los}^2\rangle(R)\,dx\,dy \Big/ \int_{\rm ap} I(R)\,dx\,dy. \tag{22}$$

Similar equations apply to the other velocity moments and to the velocity distribution $\mathcal{L}_{\rm iso}(v,R)$. In integrated light measurements one can also take the observational

point-spread-function (PSF) into account by convolving both $I(x,y)$ and $I\langle v^2_{\rm los}\rangle(x,y)$ with the PSF before evaluation of the integrals in equation (22).

In the following we write

$$\bar\sigma_{\rm los} \equiv \langle v^2_{\rm los}\rangle^{1/2}_{\rm ap}, \quad \bar\sigma_{\rm pmr} \equiv \langle v^2_{\rm pmr}\rangle^{1/2}_{\rm ap}, \quad \bar\sigma_{\rm pmt} \equiv \langle v^2_{\rm pmt}\rangle^{1/2}_{\rm ap}. \tag{23}$$

It is also useful to consider the quantity

$$\bar\sigma_{\rm pm} \equiv \langle (v^2_{\rm pmr}+v^2_{\rm pmt})/2\rangle^{1/2}_{\rm ap} = \sqrt{(\bar\sigma^2_{\rm pmr}+\bar\sigma^2_{\rm pmt})/2}, \tag{24}$$

which corresponds to the one-dimensional RMS velocity averaged over all directions in the plane of the sky. Note that velocities in the plane of the sky are not directly accessible observationally. Instead of $\bar\sigma_{\rm pmr}$ and $\bar\sigma_{\rm pmt}$ we measure proper motions $\bar\Sigma_{\rm pmr}$ and $\bar\Sigma_{\rm pmt}$ that satisfy

$$\bar\Sigma_{...}[\,{\rm mas\,yr^{-1}}] = \bar\sigma_{...}[\,{\rm km\,s^{-1}}] \,/\, (4.7404\,D[\,{\rm kpc}]). \tag{25}$$

Transformation to velocities requires an assumption about the cluster distance D.

The overlying bar in the preceding equations is used to differentiate the root-mean-square (RMS) velocity $\bar\sigma$ from the velocity dispersion σ. These quantities are equal only if the mean streaming is zero (which is always true in the pmr direction).

2.7. *Optimizing and Assessing the Fit to the Data*

In general, we will want to model line-of-sight datapoints $\bar\sigma_{{\rm los},i} \pm \Delta\bar\sigma_{{\rm los},i}$ available for $i = 1,\ldots,N$, as well as proper motion datapoints $\bar\Sigma_{{\rm pm}...,j} \pm \Delta\bar\Sigma_{{\rm pm}...,j}$ available for $j = 1,\ldots,M$ (with each proper motion data point referring to either the pmr or the pmt direction). To calculate model predictions we use the known surface brightness profile $\mu_{{\rm obs},X}(R)$ and the extinction A_X. The questions are then how to assess the fit to the data for given model parameters, and how to determine the parameters that provide adequate fits.

2.7.1. *Distance and Mass-to-Light Ratio*

Suppose that we have obtained model predictions $\hat\sigma_{{\rm los},i}$ and $\hat\Sigma_{{\rm pm}...,j}$ for the datapoints, using trial values $\hat D$ and $\hat\Upsilon$ for the distance and mass-to-light ratio, respectively. The fit can then be improved by scaling of the model predictions, which corresponds to rescaling of the mass and distance scales of the model. Let $F_{\rm los}$ and $F_{\rm pm}$ be factors that scale the model predictions in the line-of-sight and proper motion directions, respectively. The best-fitting values of these scale factors and their error bars can be calculated using the statistics

$$\chi^2_{\rm los} \equiv \sum_i [(\bar\sigma_{{\rm los},i} - F_{\rm los}\hat\sigma_{{\rm los},i})/\Delta\bar\sigma_{{\rm los},i}]^2,$$
$$\chi^2_{\rm pm} \equiv \sum_j [(\bar\Sigma_{{\rm pm}...,j} - F_{\rm pm}\hat\Sigma_{{\rm pm}...,j})/\Delta\bar\Sigma_{{\rm pm}...,j}]^2. \tag{26}$$

The best fit in each case is the value with the minimum χ^2 (i.e., $d\chi^2/dF_{...} = 0$), and the 68.3% confidence region corresponds to $\Delta\chi^2 = \chi^2 - \chi^2_{\rm min} \le 1$. The inferred scalings imply that the distance and mass-to-light ratio are optimized for $D_{\rm fit} = \hat D F_{\rm los}/F_{\rm pm}$ and $\Upsilon_{\rm fit} = \hat\Upsilon F_{\rm los} F_{\rm pm}$. These fits apply at the given values of the other model parameters, some of which are also affected by the scaling. The model parameters $M_{\rm BH}$ and $M_{\rm dark}$ are proportional to $F^3_{\rm los}/F_{\rm pm}$, and the model parameter $a_{\rm dark}$ is proportional to $F_{\rm los}/F_{\rm pm}$.

The error bars in $D_{\rm fit}$ and $\Upsilon_{\rm fit}$ (at fixed values of the other parameters) follow from propagation of the uncertainties in $F_{\rm los}$ and $F_{\rm pm}$. The errors in $F_{\rm los}$ and $F_{\rm pm}$ are uncorrelated, but the errors in $D_{\rm fit}$ and $\hat\Upsilon$ can be highly correlated or anti-correlated. We will not generally quote the correlation coefficient in this paper, but nonetheless, this should be kept in mind where necessary.

The use of scalings as described here provides a means of reducing the parameter space of the models by two. Also, it directly yields the best-fit distance and mass-to-light ratio if the remaining parameters can be determined or eliminated independently. The parameters $M_{\rm BH}$, $M_{\rm dark}$ and $a_{\rm dark}$ can be determined as described in Section 2.7.2. They primarily affect the datapoints near the cluster center. So they can also be effectively eliminated by restricting the definition of the χ^2 quantities in equation (26) to the datapoints at large radius. The anisotropy profile $\beta(r)$ can be determined as described in Section 2.7.3.

2.7.2. *Dark Mass*

Any dark component in our models can be either a cluster with parameters $(M_{\rm dark}, a_{\rm dark})$ or an IMBH of mass $M_{\rm BH}$. The latter is mathematically (but not astrophysically) equivalent to a cluster with parameters $(M_{\rm dark} = M_{\rm BH}, a_{\rm dark} = 0)$. It is therefore not possible to discriminate between an IMBH and a dark cluster of sufficiently small size (within a resolution determined by the properties of the data). Conversely, we only need to explore the $(M_{\rm dark}, a_{\rm dark})$ parameter space, and this will automatically tell us (at $a_{\rm dark} = 0$) what the limits on an IMBH are. In the following we will use the term "dark mass" to refer generically to a dark component that could be either a dark cluster as in equation (7) or an IMBH. We have not explored models that have both a dark cluster *and* an IMBH, although that would not have been difficult.

At given $\beta(r)$, we start by calculating initial guesses for $\hat D$ and $\hat\Upsilon$ by fitting only the data at large radii. We then calculate for a range of trial values $(\hat M_{\rm dark}, \hat a_{\rm dark})$ the model predictions $\hat\sigma_{{\rm los},i}$ and $\hat\Sigma_{{\rm pm}...,j}$ for all the datapoints. For each pair of trial values we calculate $D_{\rm fit}$ and $\Upsilon_{\rm fit}$ as in Section 2.7.1 by using the quantities $\chi^2_{\rm los}$ and $\chi^2_{\rm pm}$, including observations at all distances from the cluster center. We then map the contours of $\chi^2 \equiv \chi^2_{\rm los} + \chi^2_{\rm pm}$ in the two-dimensional $(M_{\rm dark}, a_{\rm dark})$ parameter space. The best fit $(M_{\rm dark,fit}, a_{\rm dark,fit})$ is obtained as the point of minimum χ^2. The uncertainties of the fit follow from standard $\Delta\chi^2$ statistics, with the 68.3% confidence region corresponding to $\Delta\chi^2 = \chi^2 - \chi^2_{\rm min} \le 2.3$ (Press et al. 1992). If there are combinations with $M_{\rm dark} = 0$ within the confidence region, then a dark mass is not required to fit the data, for the assumed $\beta(r)$. If there are combinations with $M_{\rm dark} \ne 0$ and $a_{\rm dark} = 0$ within the confidence region, then the presence of an IMBH is consistent with the data, for the assumed $\beta(r)$. If we assume that the dark mass is an IMBH, then its 68.3% confidence region is given by $\Delta\chi^2 \le 1$ at $a_{\rm dark} = 0$.

The presence of an IMBH not only increases the RMS velocity towards the center, but it also changes the shape of the velocity distribution. The distribution measured through an aperture around the center will have power-

law wings that are significantly broader than those of a Gaussian distribution (van der Marel 1994b). This leads to the possibility of detecting very high velocity stars (Drukier & Bailyn 2003). It is therefore useful to determine and analyze the observed velocity distribution of the stars around the center, to further assess the plausibility of the presence of an IMBH. The observed distribution can be compared to the predicted distribution $\mathcal{L}_{\rm iso,ap}(v)$ that can be calculated for an isotropic model. It is also useful to calculate the Gauss-Hermite moments (van der Marel & Franx 1993) of the observed velocity distribution as a function of distance from the center. A sufficiently massive IMBH causes an increase in h_4 towards the center (van der Marel 1994b). The absence of broad wings or a central increase in h_4 can be used to obtain an upper limit to the mass of any IMBH.

2.7.3. *Anisotropy Profile*

Binney & Mamon (1982) showed that there are many different combinations of $\beta(r)$ and the enclosed mass $M(< r)$ in a spherical system that can produce the same observed projected RMS line-of-sight velocity profile $\bar{\sigma}_{\rm los}(R)$. The key to constraining the mass distribution, and hence the possible presence of an IMBH, is therefore to constrain the anisotropy profile $\beta(r)$. This is not possible when only RMS line-of-sight velocities are available. However, $\beta(r)$ can be constrained when information is available on deviations of the line-of-sight velocity distributions (LOSVDs) from a Gaussian, as function of projected position on the sky (van der Marel & Franx 1993; Gerhard 1993). This information is fairly indirect, and to exploit it one must construct complicated numerical models that retrieve the full phase-space distribution function of the stars (van der Marel et al. 1998; Cretton et al. 1999; Gebhardt et al. 2000; Valluri et al. 2004; Thomas et al. 2004; van den Bosch et al. 2008). This has been explored with considerable success in the context of studies of early-type galaxies (e.g., Cappellari et al. 2007).

In the present context, high-quality proper motion data are available. It is then considerably more straightforward to constrain $\beta(r)$. This was demonstrated by Leonard & Merritt (1989), who were the first to use proper motion data to examine in detail the mass distribution in a star cluster. The function $[\bar{\Sigma}_{\rm pmt}/\bar{\Sigma}_{\rm pmr}](R)$ is a direct measure of anisotropy as seen in the plane of the sky. This ratio is independent of either the distance or the mass-to-light ratio scaling of the model. There is only a weak dependence on the presence of a dark mass (and this only affects the very central region). Therefore, the one-dimensional observed function $[\bar{\Sigma}_{\rm pmt}/\bar{\Sigma}_{\rm pmr}](R)$ tightly constrains the one-dimensional intrinsic function $\beta(r)$. In fact, for a spherical system there is a unique relation between the two (Leonard & Merritt 1989). This is the primary reason why in the present context it is possible to obtain robust results based on something as simple as the spherical Jeans equation, while much more sophisticated techniques have become standard practice for galaxies.

To build some intuitive understanding of the meaning of $[\bar{\Sigma}_{\rm pmt}/\bar{\Sigma}_{\rm pmr}](R)$, consider the case in which $\beta(r)$ is independent of radius and $j\overline{v_r^2}(r) \propto r^{-\xi}$. The relevant integrals in equation (19) can then be expressed analytically in terms of beta-functions. Their ratio is independent of radius R and simplifies to

$$[\bar{\Sigma}_{\rm pmt}/\bar{\Sigma}_{\rm pmr}] = \xi(1-\beta)/(\xi-\beta). \tag{27}$$

For small β (i.e., a system not too far from isotropy) we can use a first order Taylor approximation, which yields

$$\beta_{\rm pm}(R) = \beta(1-\frac{1}{\xi}), \tag{28}$$

where we have defined the function

$$\beta_{\rm pm}(R) \equiv 1 - \{[\bar{\Sigma}_{\rm pmt}/\bar{\Sigma}_{\rm pmr}](R)\}^2, \tag{29}$$

in analogy with the definition of $\beta(r)$. This implies that the deviation of $[\bar{\Sigma}_{\rm pmt}/\bar{\Sigma}_{\rm pmr}]$ from unity is a factor $(1-\frac{1}{\xi})$ of the deviation of $[\overline{v_{\rm tan}^2}/\overline{v_r^2}]^{1/2}$ from unity. (This uses the Taylor approximation $(1-\beta)^{1/2} \approx 1-(\beta/2)$, and similarly for $\beta_{\rm pm}$.) Hence, $[\bar{\Sigma}_{\rm pmt}/\bar{\Sigma}_{\rm pmr}(R)]$ is a "diluted" measure of the anisotropy that is present intrinsically, with dilution factor $(1-\frac{1}{\xi})$.

The approximations made above cannot be used in the core of a cluster, where $\xi = 0$. The assumption that the system remains scale free all along the line of sight is then not accurate. However, in the outer parts of a cluster the approximation is a reasonably accurate guide, with the value of ξ depending on the exact cluster structure. For example, an isothermal sphere has $\xi = 2$ at large radii, while a Plummer model has $\xi = 6$. The corresponding dilution factors $(1-\frac{1}{\xi})$ are 0.50 and 0.83, respectively. Real clusters typically fall between these extremes. More extensive analytical calculations of $\beta_{\rm pm}(R)$ are presented in, e.g., Leonard & Merritt (1989) and Wybo & Dejonghe (1995). Either way, analytical calculations are mostly useful here for illustration. In practice we calculate the integrals in equation (19) numerically.

The extent to which the velocity distribution of the stars (in either the los, pmr, or pmt direction) differs from a Gaussian provides secondary information on the amount of velocity anisotropy in the system. The modeling technique used here is insufficient to exploit this information, since we are not calculating actual phase-space distribution functions for anisotropic models (although this would in principle be possible, e.g., Dejonghe 1987; Gerhard 1993; van der Marel et al. 2000). Nonetheless, we can observationally characterize the Gauss-Hermite moments as function of projected distance from the cluster center. Also, we can calculate the predicted velocity distributions $\mathcal{L}_{\rm iso}(v,R)$ for an isotropic model, and from this the corresponding Gauss-Hermite moments. Comparison of the observed and predicted quantities provides an independent assessment of possible deviations from isotropy.

2.8. *Numerical implementation*

To apply the formalism described above we augmented a software implementation used previously in, e.g., van der Marel (1994a). The code uses a logarithmically spaced grid, from very small to very large radii (so that a negligible fraction of the cluster mass resides outside the grid). Relevant quantities are tabulated on this grid. Integrals are evaluated through Romberg quadrature (e.g., Press et al. 1992) to high numerical precision. Tabulated quantities are interpolated using cubic splines for use in subsequent integrations. This avoids the need for calculation of higher-dimensional integrals. The derivatives

dI/dR and $dj/d\Psi$ in equations (3) and (21), respectively, are calculated using finite differences. The derivative $d\Phi_{\rm tot}/dr$ in equation (16) can be manipulated analytically so that numerical differentiation is not needed. The accuracy of the code was verified by reproducing analytically known results for special potential-density pairs (e.g., Plummer models).

3. PROJECTED DENSITY PROFILE DATA

The primary input for our models is the projected radial density profile. To characterize this profile over the full range of radii spanned by ω Centauri, we have combined the ground-based measurements at intermediate and large radii collected in Trager, King & Djorgovski (1995), with the new HST measurements at small radii presented in Paper I. Much of the measurements come in the form of projected star count profiles $\nu_{\rm proj}(R)$. Our equations of Section 2 are mostly expressed in terms of the observed (or implied) surface brightness profile $\mu_{\rm obs}(R)$. The profiles $\nu_{\rm proj}(R)$ and $\mu_{\rm obs}(R)$ are uniquely related to each other (see eq. [30] below), given our assumption to neglect mass segregation among the luminous stars.

3.1. *Ground-based Data*

Trager et al. compiled literature data from various sources. We rejected from their compilation the data points to which they did not assign the maximum weight (unity in their notation). This leaves only the most reliable literature sources for ω Centauri, namely the integrated-light photo-electric measurements of Gascoigne & Burr (1956) and Da Costa (1979), and the number density measurements of King et al. (1968). All these authors presented averages for concentric circular annuli. Da Costa also presented separate measurements using a drift scan technique, which were subsequently calibrated to estimate the profile along concentric circular annuli. King et al. presented results for two separate plates from Boyden Observatory. We follow Trager et al. by referring to the different data sets with the abbreviations GBANN, DANN, DSCAN, ADH-1792, and ADH-1846; the latter two abbreviations refer to the IDs of the photographic plates analyzed by King et al. For our analysis we used the values provided by Trager et al., who calibrated the published measurements to a V-band surface brightness scale with a common zeropoint. We assigned to each data point an error bar of 0.142 mag, based on the procedure and analysis of McLaughlin & van der Marel (2005; see their Table 6). This corresponds to the scatter in the data with respect to a smooth curve.

3.2. *HST Data*

Paper I presented number density measurements for concentric circular annuli based on HST data. Considerable effort was spent to accurately determine the cluster center, and to correct the results for the effects of incompleteness. Error bars were determined from the Poisson statistics of the counted stars. Paper I discussed number density profiles for various magnitude bins, and showed that there is no strong dependence on magnitude. For the analysis presented here we have used the profile for all stars in the HST images with B-band instrumental magnitude < -10 (this is defined in Paper I and corresponds to stars measured with signal-to-noise ratio $S/N \gtrsim 100$). The choice of magnitude range was motivated by the desire to maximize the number of stars (i.e., to minimize the error bars on the density profile) while maintaining a similar mean magnitude (~ -12) as for the sample of stars for which high-quality proper motions are available from Paper I.

To extend the profile from the Trager et al. compilation to the smaller radii accessible with the HST data it is necessary to calibrate the projected number density $\nu_{\rm proj}(R)$ to a projected surface brightness $\mu_{{\rm obs},V}(R)$. It follows from equations (1), (4), (12), and (13) that

$$\mu_{{\rm obs},V}[{\rm mag\ arcsec^{-2}}] = -2.5\log(\nu_{\rm proj}[{\rm arcsec^{-2}}]) + Z, \tag{30}$$

where the zeropoint Z is equal to

$$Z = 21.572 + M_{\odot,V} + 2.5\log\{(f/\lambda[L_\odot])(\pi D[{\rm kpc}]/648)^2\}, \tag{31}$$

where $M_{\odot,V} = 4.83$ (Binney & Merrifield 1998). Although $(f/\lambda[L_\odot])$ can in principle be estimated, we have found it more reliable to calibrate Z so that the surface brightness profiles from Trager et al. and Paper I agree in their region of overlap. We have done this by including Z as a free parameter in the fits described below, which yields $Z = 18.21$. For a canonical distance $D = 4.8$ kpc (vdV06) this implies that $(f/\lambda[L_\odot]) = 1.0$. With this Z there is excellent agreement between the different datasets, as shown in Figure 1a.

NGB08 studied the surface brightness profile of unresolved light in ω Centauri using HST images. In principle, the advantage of using unresolved light over star counts is that one can trace the cumulative effect of all the unresolved faint stars, rather than counting only the less numerous resolved ones. However, we showed in Paper I that even at HST resolution, the unresolved light is dominated by scattered light from the PSF wings of only the brightest stars. So in reality, the inherent statistics of unresolved light measurements are poorer than those of star count measurements. Moreover, we showed in Paper I that the combined photometric and kinematic center of ω Centauri is actually $12''$ away from the position where NGB08 identified it to be. There is no simple way to transform their measurements over concentric annuli to a different center position. For these reasons, we have not included the NGB08 surface brightness datapoints in the dataset used for the dynamical modeling.

4. PROJECTED DENSITY PROFILE MODELS

It is important for the modeling to have a smooth representation of the projected intensity profile $I(R)$, since the derivative dI/dR is needed in equation (3) for the calculation of $j(r)$. For the dynamical modeling we have used a parametric approach, although this can in principle be done non-parametrically (e.g., Gebhardt & Fischer 1995). We have fit the data using a smooth function of the form

$$I_{\rm obs}(R) = I_b\, 2^{(\eta-\gamma)/\alpha}\, (R/b)^{-\gamma} \left[1+(R/b)^\alpha\right]^{-(\eta-\gamma)/\alpha} \left[1+(R/c)^\delta\right]^{-(\epsilon-\eta)/\delta} \tag{32}$$

This functional form has no particular physical significance, but it is useful because it can fit a wide range of observed profiles. The profile has a power-law cusp $I \propto R^{-\gamma}$ at radii $R \ll b$. It then breaks to a logarithmic

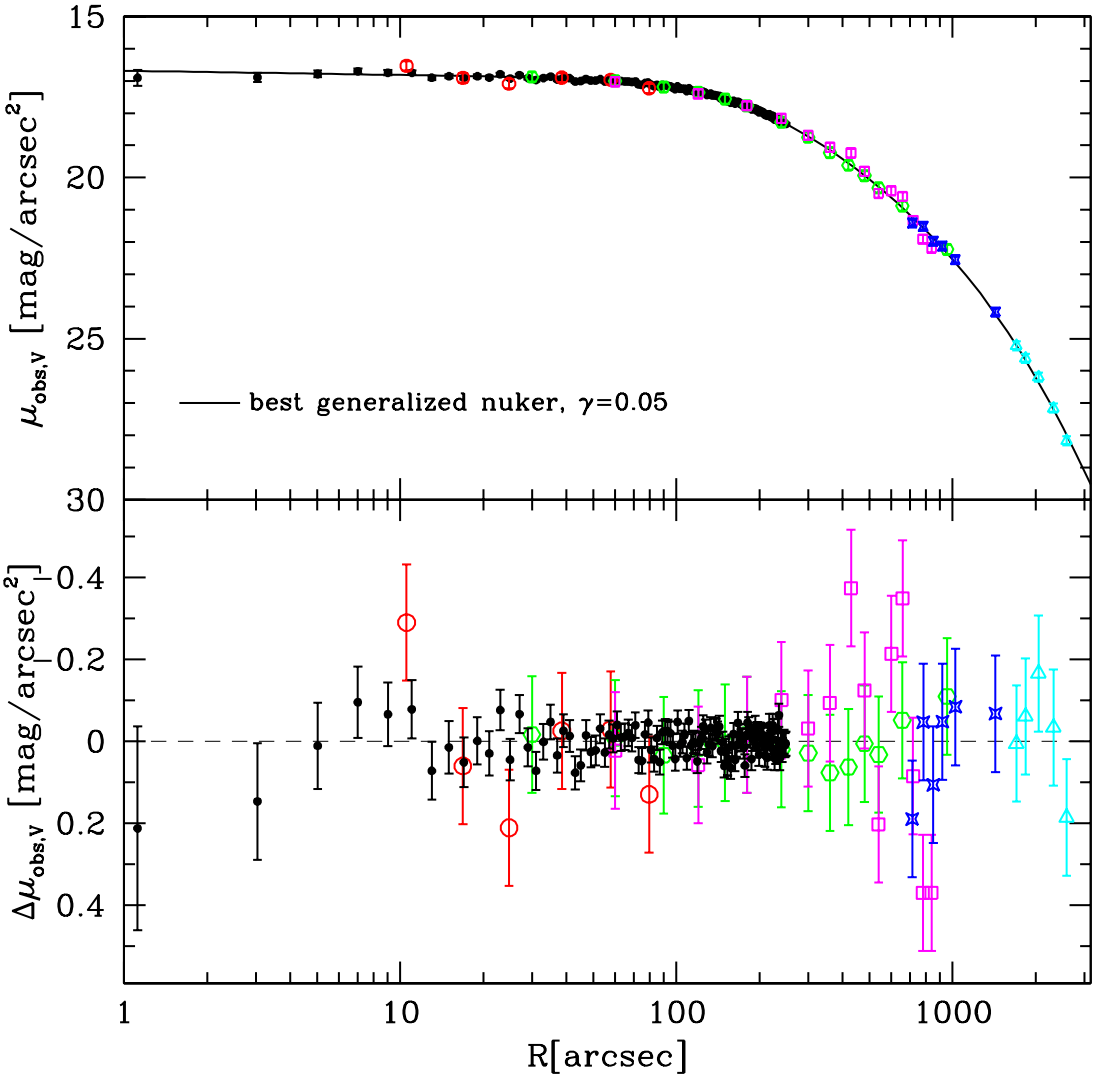

FIG. 1.— (a; top panel) V-band surface brightness profile of ω Centauri in mag arcsec^{-2} versus radius in arcsec. Data points are from various sources as described in the text. The curve is our best model fit of equation (32), which has a central cusp slope $\gamma = 0.05$. (b; bottom panel) Residuals of the fit in the top panel. The small solid dots (black in the on-line version) are the HST star count data from Paper I. The bigger open symbols are from the compilation of ground-based data in Trager et al. (1995), as described in the text: GBANN, hexagons (green); DANN, circles (red); DSCAN, squares (magenta); ADH-1792, triangles (cyan); ADH-1846, crosses (blue).

slope η at $R \approx b$, and further to a logarithmic slope ϵ at $R \approx c > b$. The parameters α and δ measure the sharpnesses of the breaks. The intensity I_b, corresponding to a magnitude μ_b through equation (1), sets the overall intensity scale. The profile is similar to a so-called "nuker" profile (Lauer et al. 1995), but with two breaks instead of just one. We will refer to it as a generalized nuker profile.

The best fit to the dataset presented in Section 3 was determined using a Levenberg-Marquardt iteration scheme (Press et al. 1992). It has parameters $\mu_b = 17.74$, $b = 183.1''$, $c = 2158''$, $\gamma = 0.05$, $\eta = 2.37$, $\epsilon = 10.00$ (the maximum value allowed during the iteration), $\alpha = 2.29$, and $\delta = 1.70$. The fit and its residuals are shown in Figure 1. The quality of the fit is excellent. For the subset of the data from Paper I, the $\chi^2 = 130.5$ for 125 datapoints with an RMS residual of 0.04 mag. The total $\chi^2_{\rm min} = 169.3$ for all 159 datapoints, corresponding to 151 degrees of freedom. This is acceptable at the $\sim 1\sigma$ level for a χ^2 distribution. The residuals appear generally consistent with random scatter in line with the error bars, with little evidence for systematic trends.

The best fit has a central cusp slope of $\gamma = 0.05$. To determine the statistical error on this value we also performed a range of fits in which γ was fixed a priori, while all other parameters were varied to optimize the fit. The central structure of our best fit for $\gamma = 0$ is shown in Figure 2 for comparison to our overall best fit. The curve of $\Delta\chi^2 \equiv \chi^2 - \chi^2_{\rm min}$ as function of γ was used to derive the error bar on γ, which yields $\gamma = 0.05 \pm 0.02$.

When using a generalized nuker fit, a constant surface brightness core is inconsistent with the data at $\sim 2.5\sigma$ confidence. However, this parameterized approach may not yield an unbiased estimate of the asymptotic slope γ at the smallest radii. The data at all radii are given equal weight in the χ^2 of the fit, but it is obviously only the data near the very center that contain most of the relevant information on γ. Also, the two breaks at radii b and c in the generalized nuker profile fit correspond to the breaks associated with the traditional core and tidal radii of ω Centauri. The parameterization does not have sufficient flexibility to reproduce any possible change in

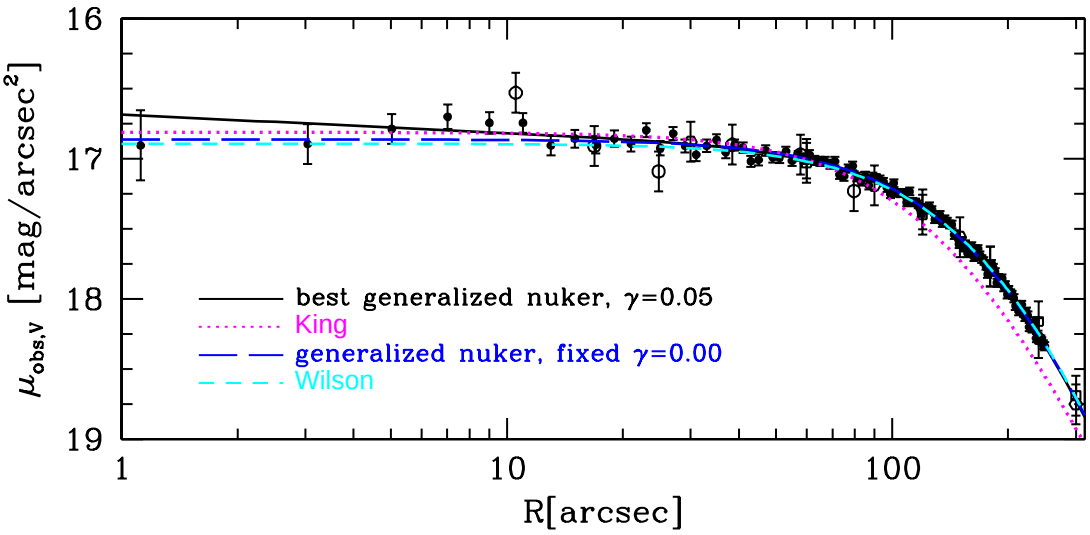

FIG. 2.— V-band surface brightness profile of ω Centauri in mag arcsec^{-2} versus radius in arcsec. The data and the symbols are the same as in Figure 1a, but this figure focuses more on the central region. The solid curve (black in the on-line version) is the overall best model fit of equation (32), which has a central cusp slope $\gamma = 0.05$. The long-dashed curve (blue) is the best fit when the cusp slope is fixed a priori to $\gamma = 0$. The dashed (cyan) and dotted (magenta) curves are the Wilson and King models, respectively, presented in McLaughlin & van der Marel (2005). These were tailored to fit the compilation of ground-based data in Trager et al. (1995).

profile slope well within the core radius ($r_0 = 141^{+7}_{-13}$ arcsec; McLaughlin & van der Marel 2005).

An alternative and simpler approach to determine γ is to fit a straight line to the $(\log R, \log I)$ data at $R \leq R_{\rm max}$. For $R_{\rm max} = 15''$, this yields $\gamma = 0.00 \pm 0.07$. The values of γ inferred for other values of $R_{\rm max}$ in the range 0–20$''$ are in statistical agreement with this. This analysis indicates that the central data points are consistent with a flat core.

An additional assessment of models with a flat core can be obtained from comparison of the new data with previously published models. McLaughlin & van der Marel (2005) presented detailed surface brightness fits for a large sample of galactic and extragalactic globular clusters. They considered three types of models with decreasing amounts of diffuse outer structure, the power-law model, the Wilson (1975) model, and the King (1966) model. The power-law models are similar to the parameterizations that we have used here, but with a more restricted subset of the parameters (namely, $\gamma = 0$, $\alpha = 2$, and $c = \infty$ were kept fixed). The models from Wilson and King are both based on a parameterized isotropic phase-space distribution function. The Wilson prescription differs from the better known King models in that it uses a slightly different lowering of the exponential energy distribution, so as to produce a model that has a more extended but still finite outer structure. McLaughlin & van der Marel discussed ω Centauri as a special example (their section 4.2.1) and found that it is well fit by a Wilson model, but less so by a King model. The central structure of both models is shown in Figure 2. The Wilson model is very similar to our best fit model with fixed $\gamma = 0$. The King model is also similar at radii $R \lesssim 100''$, but it under-predicts the brightness at intermediate radii (before improving again at larger radii, not shown in Figure 2).

The Wilson and King models shown in Figure 2 are the ones that were previously fit by McLaughlin & van der Marel to the Trager et al. data. At small radii these models represent an extrapolation of the ground-based data under the assumption of a constant surface brightness core. Although the models were not fit to the HST data, they do provide a perfect fit to the two innermost HST star count data points. By contrast, our own best generalized nuker model fit with $\gamma = 0.05$ over-predicts both of the innermost datapoints by about 1σ. The fact that $\gamma = 0.05$ is preferred in our fits over $\gamma = 0$ is therefore because it fits better the data at radii $R \approx 10''$, and not because it provides the best fit closest to the center.

NGB08 inferred from their HST study of integrated light in ω Centauri that it has a central cusp slope $\gamma = 0.08 \pm 0.03$. At first glance, this result appears consistent with that from our generalized nuker fit. However, since they did not measure the brightness profile around the same cluster center, the agreement between our inferred cusp slopes is likely coincidental.

In summary, we conclude that the central cusp slope of ω Centauri is $\gamma \lesssim 0.07$ at $\sim 1\sigma$ confidence. That is, we interpret the $\gamma = 0.05 \pm 0.02$ from our generalized nuker fit as an upper limit. We do this because it over-predicts the central two data points, and because other statistics do not show evidence for a non-zero slope. In the dynamical analysis that follows we specifically consider two generalized nuker fits that span the range of possibilities: models with a shallow cusp ($\gamma = 0.05$) and models with a constant density core ($\gamma = 0$). We will refer to these as cusp models and core models, respectively. In all calculations we have transformed the observed intensity $I_{{\rm obs},V}(R)$ to an extinction-corrected intensity $I_V(R)$ using equation (2) with $A_V = 0.372$ for ω Centauri (McLaughlin & van der Marel 2005).

5. KINEMATICAL DATA

To constrain the parameters of the dynamical models we need to use both line-of-sight and proper motion data at a range of radii. For this we have combined ground-based line-of-sight and proper motion data at intermediate and large radii with the new HST proper motion

data at small radii presented in Paper I.

We construct spherical models to interpret the data. These models yield only a single radial profile for each projected quantity, with no azimuthal variations from the observed major axis of ω Centauri to its observed minor axis. To get accurate results for the model parameters, it is important that these models be used to reproduce the *average* radial variations seen in the data. This is achieved by using for each projected quantity that is fit the average of the measurements along concentric annuli. This is indeed what we extracted for the projected density in Section 3, and we therefore do the same here for the projected velocity distributions. When averages are taken over annuli, all the odd moments of the velocity distribution are zero. Of primary interest here are the second moments, which yield the RMS velocity $\bar{\sigma}_{\rm los}$ and the RMS proper motions $\bar{\Sigma}_{\rm pmr}$ and $\bar{\Sigma}_{\rm pmt}$.

In reality, variations do exist between observed quantities along the major and minor axis. vdV06 discussed this in detail for the existing ground-based data. In Appendix B we address this for the new HST proper motion data. In particular, the RMS proper motions are not the same along the major and minor axes, and the RMS proper motions in the major and minor axis directions on the sky are not the same. Also, the mean proper motion in the transverse (pmt) direction is not zero (vdV06; Section 5.2.3; Appendix C). By modeling these issues it is possible to constrain, e.g., the cluster inclination and its rotation rate. However, it is not essential to model these issues to achieve a good understanding of the central mass distribution, which is the main goal here.

5.1. *Ground-based Data*

5.1.1. *Line-of-Sight Kinematics*

vdV06 compiled line-of-sight velocity data of individual stars in ω Centauri. The original data were obtained by Suntzeff & Kraft (1996), Mayor et al. (1997), Reijns et al. (2005), and Gebhardt et al. (in preparation). vdV06 performed various operations and cuts to homogenize and correct the data as necessary for dynamical modeling. This included: improved removal of cluster non-members; removal of stars with low enough brightness or large enough velocity error bars to make their reliability suspect; application of additive velocity shifts to correct for offsets in velocity zero-points between data sets; multiplicative rescaling of the velocity error bars where necessary, as dictated by actual measurements of scatter between repeat measurements; subtraction of the systemic line-of-light velocity; and subtraction of the apparent solid-body rotation introduced into the velocity field through the combination of systemic transverse motion and large angular extent ("perspective rotation"). This produced a final homogenized sample of line-of-sight velocities for 2163 stars with uncertainties below $2.0\,{\rm km\,s^{-1}}$.

Glenn van de Ven kindly made the homogenized sample from vdV06 available to us for use in our data-model comparisons. To determine the profile of $\bar{\sigma}_{\rm los}(R)$ we binned the stars in radius and then used the statistical methodology described in Appendix A. Radii were calculated with respect to the center determined in Paper I, which differs by $15.5''$ from the center used by vdV06 (which was determined by van Leeuwen et al. 2000). We chose a central bin of $20''$ radius (with 25 stars) for maximum resolution near the center, and then chose the remaining bins to contain 200 stars each.

Sollima et al. (2009) obtained line-of-sight velocities of 318 cluster members at large radii, which they merged with observations closer to the center by Pancino et al. (2007). This yielded a homogeneous sample of 946 cluster members, from which they derived the profile $\bar{\sigma}_{\rm los}(R)$. Seitzer (1983) presented the $\bar{\sigma}_{\rm los}(R)$ profile derived from 118 clusters members with known velocities at a range of radii. We included the published profiles from both studies in our data-model comparisons. For each study we averaged the first two bins in the profile together, since the first bin had a large error bar and did not provide spatial resolution that competes with the vdV06 compilation.

Scarpa et al. (2003) obtained line-of-sight velocities of 75 cluster members at large radii. From this they determined the velocity dispersion $\sigma_{\rm los}$ in four radial bins. The stars were limited to the West side of the cluster, so the results do not represent averages over a complete annulus on the sky. Nonetheless, we included these observations in our data-model comparisons. We subtracted in quadrature from the published $\sigma_{\rm los}$ values the average measurement error of $1\,{\rm km\,s^{-1}}$. To obtain $\bar{\sigma}_{\rm los}$ we added in quadrature $V^2/2$, where V is the rotation velocity amplitude quoted in Scarpa et al. (2003); the factor $1/2$ is the average of a squared sinusoidal variation over a full range of angles.

The profiles obtained from the Sollima et al. (2009), Seitzer (1983), and Scarpa et al. (2003) observations do not pertain to the same center as that inferred in Paper I. However, the smallest radial bin that we use from these studies is the 4 arcmin diameter combined central bin of Sollima et al. A center offset of $15.5''$ (as applicable to the Sollima et al. and Scarpa et al. results, who used the van Leeuwen et al. 2000 center) should not significantly affect statistics calculated over bins that extend to such large distances from the center.

At small radii we used as additional data points the integrated-light measurements from NGB08. They inferred velocity dispersions over square fields of $5'' \times 5''$. Because of the significant size of these fields, we did not include the impact of PSF convolution in our model predictions for these data. We placed the measurements at the distance from the cluster center inferred in Paper I, which is $12''$ for both fields. We cannot use the data to calculate a true average over an annulus. However, we do have two measurements at the same distance from the center at a 60° angle. Including both measurements in our model fits is in low-order approximation similar to fitting the average over an annulus.

NGB08 did not measure the mean velocity over their fields as compared to the systemic velocity. Hence, their measurements are dispersions $\sigma_{\rm los}$ rather than RMS velocities $\bar{\sigma}_{\rm los}$. However, it is known from previous observations (e.g., vdV06) that $V_{\rm los}/\sigma_{\rm los}$ in ω Centauri decreases towards the center. This ratio is small enough at the position of the NGB08 fields that $\bar{\sigma}_{\rm los} \approx \sigma_{\rm los}$ to high accuracy (see Section 5.2.3 for a quantitative estimate).

Figure 3a shows the collected $\bar{\sigma}_{\rm los}$ data from all the sources, as function of projected distance R from the cluster center. The different data sets match well in their regions of overlap.

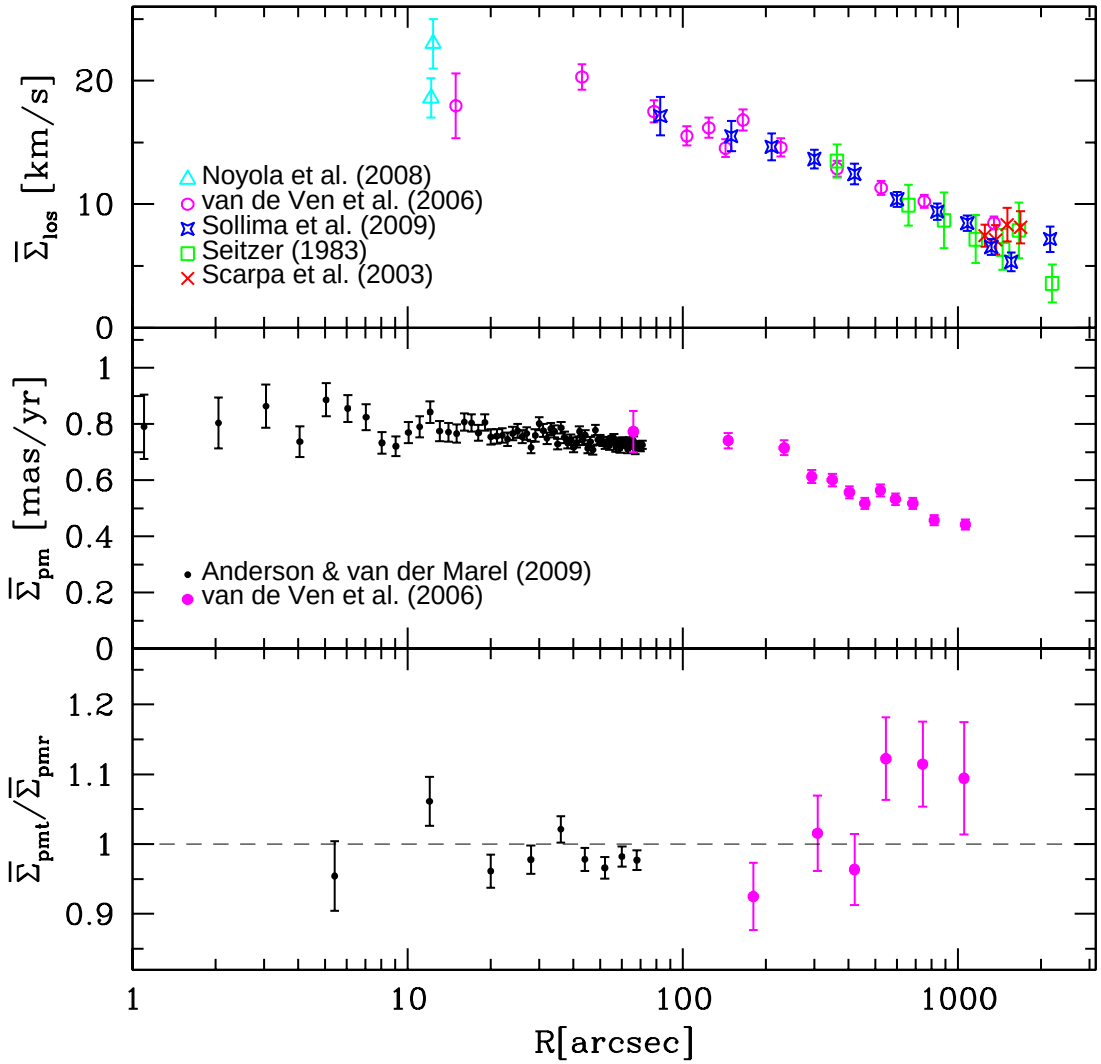

FIG. 3.— Observed kinematical quantities for ω Centauri as function of projected radius R from the cluster center. Data points are based on analysis of various sources described in the text: circles (magenta in the on-line version) are based on vdV06, which is itself a compilation of line-of-sight data from Suntzeff & Kraft (1996), Mayor et al. (1997), Reijns et al. (2005), and Gebhardt et al. (in prep.), and proper motion data from van Leeuwen et al. (2000); triangles (cyan) are based on NGB08; stars (blue) are based on Sollima et al. (2009); squares (green) are based on Seitzer (1983); crosses (red) are based on Scarpa et al. (2003); and small dots (black) are based on the HST data from Paper I. Some error bars are of similar size as the plot symbols. Data from all ground-based sources except NGB08 were multiplied by a factor 1.023 to correct to same the characteristic main-sequence stellar mass as for the HST sample (see Section 5.1.3). (a; top panel) RMS line-of-sight velocity $\bar{\sigma}_{\rm los}$ in km/s (data indicated with open symbols). (b; middle panel) RMS proper motion $\bar{\Sigma}_{\rm pm}$ in mas/yr, averaged over all directions in the plane of the sky, as defined by equation [24] (data indicated with closed symbols). (c; bottom panel) Ratio $\bar{\Sigma}_{\rm pmt}/\bar{\Sigma}_{\rm pmr}$ of the RMS motions in the tangential and radial proper motion directions (data indicated with closed symbols). The RMS quantities in each dataset are averages over adjacent circular annuli. The extent of the annulus for data point i can be assessed by taking half the distance between adjacent datapoints, $\Delta R_i \approx (R_{i+1} - R_{i-1})/2$.

5.1.2. *Proper Motion Kinematics*

Ground-based proper motion data are available from van Leeuwen et al. (2000). vdV06 performed various operations and cuts to optimize and correct the data as necessary for dynamical modeling. This included: improved removal of cluster non-members; removal of stars with low enough brightness, large enough velocity error bars, or neighbors that are nearby enough to make their reliability suspect; and subtraction of the apparent solid-body rotation introduced by perspective rotation, and other spurious solid body rotation components. This produced a final sample of proper motions for 2295 stars with uncertainties below $0.2\,{\rm mas\,yr^{-1}}$ (i.e., $4.6\,{\rm km\,s^{-1}}$ at the canonical distance $D = 4.8\,{\rm kpc}$).

Glenn van de Ven kindly made the homogenized sample from vdV06 available to us for use in our data-model comparisons. Proper motions were given along the major and minor axis directions. For each star we transformed this into proper motions in the radial (pmr) and tangential (pmt) directions. We then determined the profiles of $\bar{\Sigma}_{\rm pmr}(R)$ and $\bar{\Sigma}_{\rm pmt}(R)$ by binning the stars in radius and using the statistical methodology described in Appendix A. Radii and proper motion coordinate transformations were calculated with respect to the center determined in Paper I. We chose a central bin of 90″ radius (with 30 stars) for maximum resolution near the center, and then chose the remaining bins to contain 200 stars each. We followed vdV06 by excluding the 65 outermost stars with radii $R \sim 20$–30 arcmin.

For fitting models to the data we always use the quan-

tities $\bar{\Sigma}_{\rm pmr}$ and $\bar{\Sigma}_{\rm pmt}$. However, for visualizing the results we have found it more convenient to use the quantities $\bar{\Sigma}_{\rm pm}$ and $\bar{\Sigma}_{\rm pmt}/\bar{\Sigma}_{\rm pmr}$. The RMS proper motion $\bar{\Sigma}_{\rm pm}$ averaged over all directions in the plane of the sky can be calculated directly through its definition in equations (24) and (25). In practice, we found it more convenient to calculate it by applying the statistical methodology described in Appendix A on the *combined* array of the pmr and pmt data points. For visualization of the ratio $\bar{\Sigma}_{\rm pmt}/\bar{\Sigma}_{\rm pmr}$ we adopted a radial binning scheme with 400 stars in each bin, to obtain smaller and more useful error bars.

Figure 3b shows the $\bar{\Sigma}_{\rm pm}$ data as function of projected distance R from the cluster center, and Figure 3c shows the $\bar{\Sigma}_{\rm pmt}/\bar{\Sigma}_{\rm pmr}$ data. The velocity distribution is close to isotropic near the center, but with some radial anisotropy. There is a significant increase in tangential anisotropy at a few core radii. The latter is mostly due to the contribution of rotation to the second moment $\bar{\Sigma}_{\rm pmt}$. The anisotropy in the proper motion *dispersions* is much less (King & Anderson 2002).

5.1.3. *Dependence of Kinematics on Stellar Mass*

Luminous stars in a cluster undergo two distinct effects as a result of two-body relaxation: mass segregation and energy equipartition. These effects are intimately connected through basic dynamical theory, but from an observational perspective it is useful to think of them as separate effects. Mass segregation causes stars of different masses to have slightly different spatial distributions. In Section 2 we assumed that this could be neglected when parameterizing the run of mass-to-light ratio with radius, and when connecting star count data at small radii to surface brightness data at large radii. This assumption was motivated by the absence of high-quality data to constrain the amount of mass segregation over the full scale of the cluster, and by the desire to minimize the number of a priori model assumptions. Energy equipartition causes stars of low mass to move faster than those of high mass. We measured in Paper I that low-mass stars in ω Centauri do indeed move faster than high-mass stars, albeit by less than would be predicted for complete energy equipartition ($v \propto m^{-0.5}$). Since we have a direct measurement of this, there is no reason to ignore this effect in the modeling. We therefore correct for it when comparing the observed kinematics from different data sets.

The available discrete ground-based line-of-sight and proper motion data all pertain to relatively bright stars. The apparent magnitudes of these stars place them on the giant or sub-giant branch. Since stellar evolution proceeds relatively rapidly after the main-sequence turn-off, these stars all have essentially the same mass as the main-sequence turn-off. By contrast, the stars in our new HST proper motion sample from Paper I (discussed in detail in Section 5.2 below) extend from about the main-sequence turn-off to ~ 3 magnitudes below that. From the analysis of Paper I it follows that the RMS proper motion of stars at the average magnitude of the HST sample is $\sim 2.3\%$ higher than that at the main-sequence turn-off.

For a fair comparison to the new HST proper motion data, we took the kinematics from the discrete velocity studies in Sections 5.1.1 and 5.1.2 and multiplied them by a factor 1.023. This implies that we use the observed (sub-)giant star kinematics to estimate the kinematics of lower-mass stars in the same general population. We assume implicitly that the variation of RMS kinematics with mass is the same everywhere in the cluster (although it was only measured near the cluster center), and that it applies also in the line-of-sight direction (although it was only measured in the proper motion direction). In reality, one would expect the relation between mass and velocity dispersion to change with radius, since relaxation proceeds faster near the cluster center than further out. This was neglected in the present context by applying the same small correction throughout the cluster. This was motivated in part by the fact that our study focuses mostly on the central part of the cluster anyway, but also by the fact that we didn't actually detect a difference in equipartition in Paper I between the different (central and major axis) fields for which we obtained proper motions. We did not apply the multiplicative correction to the NGB08 data. Their measurements are based on integrated light, excluding the brightest regions in their fields. It is therefore not obvious that their measurements would be dominated by (sub-)giant stars. Either way, a 2.3% correction would be much less than the error bars on their datapoints.

In summary, we are using our Jeans models to fit the kinematics of stars with masses typical of our HST proper motion sample. We extend our actual HST kinematics to larger radii using ground-based kinematics that have been corrected to the same characteristic mass. We model the cluster density profile using HST star counts for a sample that is also centered on the same characteristic mass (see Section 3.2). We make the simplifying assumption that there is no mass segregation among the luminous stars only so that we can extend the HST density profile to larger radii, where it can be tied to ground-based star-count data and integrated photometry that are based largely on giant stars (see Section 3.1). Since this approximation does not affect the very central region of the cluster, it should have little effect on our results for the central mass distribution. In fact, the multiplicative correction of 1.023 discussed above also has little effect on this. We verified explicitly that none of the main conclusions of our paper change at a level that exceeds the formal uncertainties when the multiplicative correction is omitted.

5.2. *HST Proper Motion Data*

5.2.1. *Sample selection*

In Paper I we derived proper motions for stars observed in two fields observed by HST, a "central field" on the cluster center, and a "major axis field" positioned adjacent to it in non-overlapping fashion roughly along the cluster major axis. Here we use the "high-quality" sample presented in Paper I, which contains the non-saturated stars that are isolated enough and bright enough (B-band instrumental magnitude < -11) for a particularly reliable proper motion measurement. This sample has 53382 stars in the central field and 19593 stars in the major axis field. In this sample, 95.1% of the stars have proper motion errors below $0.2\,{\rm mas\,yr^{-1}}$. Our cut in proper motion accuracy is therefore not very different from that applied by vdV06. However, the median

proper motion error per coordinate in the final sample of vdV06 is $\sim 0.14\,\mathrm{mas\,yr^{-1}}$, whereas it is a factor two smaller, $0.07\,\mathrm{mas\,yr^{-1}}$, for our sample. We note that our use of only the high-quality sample is rather conservative. Even the remainder of the sample of Paper I is quite accurate, and could well have been used to constrain the cluster dynamics.

The central HST field covers radii $R \leq 147.4''$, while the major axis field covers radii $99.7'' \leq R \leq 347.1''$. The central field has complete position angle coverage out to $R = 71.7''$ (the radius of the largest enclosed circle). For $71.7'' \leq R \leq 147.4''$ the coverage over the range of position angles becomes increasingly sparse. The major axis field is restricted at all radii to position angles within 48.5° of the major axis. For the analysis of the present paper it is important to have coverage of all position angles at a given radius, so that average kinematical quantities over circular annuli can be calculated. For this reason we have used only the 25194 stars at $R \leq 71.7''$ to constrain the dynamical models.

In our analysis we ignore the 47781 stars with high-quality HST proper motions at radii $71.7'' \leq R \leq 347.1''$. We do discuss relevant quantities derived from these data in Appendix C. More sophisticated axisymmetric modeling techniques (such as those in vdV06; van den Bosch et al. 2006; and Chaname, Kleyna, & van der Marel 2008) that might be applied in the future probably would not want to exclude these data in their analysis. By contrast, to include these data in our spherical models would require estimates of the ratios $\mathcal{R}$ of the average of either $\bar{\Sigma}_{\rm pmr}$ or $\bar{\Sigma}_{\rm pmt}$ over a restricted range of position angles, to its average over a circle. We have experimented with such estimates, but concluded that the approximations that need to be made introduce sufficient uncertainties that these data do not really help to constrain our models. Conversely, we have found no evidence that inclusion of the HST data at $71.7'' \leq R \leq 347.1''$, combined with reasonable estimates for the ratios $\mathcal{R}$, would alter in any way the conclusions draw below (see Appendix C).

To reject cluster non-members we created scatter plots of total two-dimensional proper motion $|\vec{p}|$ versus radius R, where $\vec{p}$ is the proper motion vector of an individual star. Such a plot reveals a sparse population of field stars at large values of $|\vec{p}|$, in addition to the numerous cluster stars at low $|\vec{p}|$. We rejected those stars from the sample that reside at $R > 10''$ and for which $|\vec{p}| > 2.8 - (r/500'')\,\mathrm{mas\,yr^{-1}}$. At the radii for which we have HST proper motions, this equation is a good approximation to the escape velocity curve for a spherical model with a canonical distance and mass-to-light ratio ($D = 4.8\,\mathrm{kpc}$, $\Upsilon_{\rm V} = 2.5$; vdV06). With this criterion, only 27 non-member stars were identified at $R \leq 71.7''$, the closest of which resides at $R = 21.4''$. Since the presence of an IMBH may result in the presence of rapidly moving stars at small radii, we did not reject any stars at $R \leq 10''$. The wings of the observed velocity distribution at small radii are discussed in detail in Section 6.7 below.

Our final HST proper motion sample for the dynamical modeling consists of 25167 stars. This is a factor ~ 11 larger than the number of stars with proper motions in the vdV06 sample. Most of their stars reside at larger radii than those sampled here. At the radii $R \leq 71.7''$ of our sample, vdV06 had only some two dozen stars with proper motions, and ~ 270 stars with line-of-sight velocities. The HST data therefore provide a major advance for constraining dynamical models, especially as it pertains to the gravitational influence of a possible IMBH at small radii.

5.2.2. *RMS Proper Motions*

For each star in the HST sample we decomposed the observed proper motion vector $\vec{p}$ into components in the pmr and pmt directions, respectively. We then binned the stars in radius and derived the profiles $\bar{\Sigma}_{\rm pmr}(R)$, $\bar{\Sigma}_{\rm pmt}(R)$, and $\bar{\Sigma}_{\rm pm}(R)$. We did this in similar fashion as for the ground-based proper motion data discussed in Section 5.1.2, using the statistical methodology described in Appendix A.

Figure 3b shows the $\bar{\Sigma}_{\rm pm}$ data as function of projected distance R from the cluster center. The results match well with those from vdV06 in the region where the data sets overlap. For the individual data points of $\bar{\Sigma}_{\rm pmt}$, $\bar{\Sigma}_{\rm pmr}$ and $\bar{\Sigma}_{\rm pm}$ we used binning in annuli that are $1''$ wide. For the central aperture we used a circle of radius $1.55''$, which gives an average radius $R = 1.1''$ for the datapoints enclosed by it. This central aperture is larger than the $\sim 1''$ uncertainty in the position of the cluster center derived in Paper I. This uncertainty should therefore not significantly affect the inferred kinematics. The adopted binning gives acceptably small error bars in all apertures, without losing too much spatial resolution near the center.

One immediate result from the inferred $\bar{\Sigma}_{\rm pm}(R)$ profile is that there is no strong increase towards the center, consistent with arguments presented in Paper I. A straight line fit to the $(R, \bar{\Sigma}_{\rm pm})$ data for $R \leq R_{\rm max}$, with $R_{\rm max} = 15''$, yields a slope of $-0.06 \pm 0.08\,\mathrm{km\,s^{-1}\,arcsec^{-1}}$. The slopes inferred for other values of $R_{\rm max}$ in the range 0–$20''$ are statistically consistent with this. This analysis indicates that the central data points are consistent with a flat profile of RMS velocity as function of radius.

The error bars on the observed RMS velocities can be reduced by increasing the amount of binning. For the ratio of $\bar{\Sigma}_{\rm pmt}/\bar{\Sigma}_{\rm pmr}$ shown in Figure 3c we used binning in annuli of $8''$ wide, so that even small deviations from isotropy can be measured. As for $\bar{\Sigma}_{\rm pm}$, the results match well with those from vdV06 in the region where the data sets overlap. The average over all HST data points is $\bar{\Sigma}_{\rm pmt}/\bar{\Sigma}_{\rm pmr} = 0.983 \pm 0.006$. Hence, there is a very small, but significant, amount of radial anisotropy in the central arcminute of ω Centauri.

5.2.3. *Proper Motion Rotation*

Our data calibration of Paper I (see discussion in Section 3.6.4 of that paper) removed by necessity any possible solid-body rotation component from the data. This is because we did not have access to stationary background sources in the HST fields, as would be required to measure absolute motions. This calibration has the advantage that it automatically removes any perspective rotation present in the actual proper motions (however, this is negligible for the small radii $R \leq 71.7''$ sampled by our data anyway; $\leq 0.0035\,\mathrm{mas\,yr^{-1}} = 0.08\,\mathrm{km\,s^{-1}}$ at the canonical $D = 4.8\,\mathrm{kpc}$). But of course, it has the disadvantage that it also removes a solid-body rotation fit to the actual rotation field of the cluster. This is a fundamental limitation of the data. However, we discuss

below that this has only negligible importance for our models.

In Paper I, we also used a "local correction" that removed all other mean systematic motions (as opposed to random motions) from the proper motion data. However, that was by choice, and not by necessity. The motivation for this is to calibrate out small time-variations in the higher-order geometric distortion terms. This improves the measurement of the random motions in the cluster. However, one would of course not want this to remove an important signal that is present in the data, and in particular, any possible differential rotation in the plane of the sky (i.e., the part of the rotation field that remains after subtraction of a solid-body fit). We tested for such differential rotation in Paper I, and found that it is negligible in the central HST field. Proper motion rotation curves (the mean tangential motion as function of radius) derived from data with and without the local correction agree to within $1\,\mathrm{km\,s^{-1}}$ at all radii. Therefore, solid-body rotation is the *only* unrepresented rotation component that could affect the modeling.

In principle, the loss of information on solid-body rotation can be partly recovered as in vdV06. They use the fact that for an equilibrium axisymmetric system the equation

$$V_{\rm los} = 4.7404\, D[\,\mathrm{kpc}]\, \tan i\, \mathcal{V}_{\rm y} \qquad (33)$$

must hold everywhere on the projected plane of the sky. Here i is the inclination, y the projected minor axis direction, and the symbol $\mathcal{V}$ is used to distinguish a mean proper motion from a mean velocity V. However, to use this equation with accuracy for our HST proper motions would require many more stars with line-of-sight velocities than are actually available at $R \leq 71.7''$.

The pmr direction is perpendicular to the direction of absolute rotation, and our estimates of $\bar{\Sigma}_{\rm pmr}$ are therefore not affected by our inability to measure absolute rotation. Also, in an equilibrium system there cannot be mean streaming in the pmr direction, when averaged along a circle. However, our calculated values of $\bar{\Sigma}_{\rm pmt} = (\mathcal{V}^2_{\rm pmt} + \Sigma^2_{\rm pmt})^{1/2}$ will be systematically low by a multiplicative factor $g \leq 1$, because we are unable to include any actual solid-body contribution from $\mathcal{V}^2_{\rm pmt}$. The proper motion data presented by vdV06 *did* include measurements of absolute rotations in the plane of the sky. Figure 4 shows for their data the ratios $\mathcal{V}_{\rm pmt}/\Sigma_{\rm pmt}$ and $g \equiv \Sigma_{\rm pmt}/\bar{\Sigma}_{\rm pmt}$, where the quantities in the nominator and denominator are all averages over an annulus. These measurements allow us to estimate the value of g for the HST data. The central data point shows explicitly that there is very little rotation in ω Centauri at the radii of our central HST field. More generally, in the central 10 arcmin, the rotation rate is approximately linear with radius, $\mathcal{V}_{\rm pmt}/\Sigma_{\rm pmt} \approx R/750''$. Therefore, $g \approx [1 + (R/750'')^2]^{-1/2}$. These approximations are shown as solid lines in the figure. This approximation implies that $0.995 \leq g \leq 1$ for the radii $R \leq 71.7''$ pertaining to the HST sample.

Given what is already known about proper motion rotation from the vdV06 data, our estimates of $\bar{\Sigma}_{\rm pmt}$ should be quite accurate. This is despite the fact that any solid-body part of the $\mathcal{V}_{\rm pmt}$ field cannot be measured directly in the HST data. In particular, the value of g is insufficient to explain the observed anisotropy

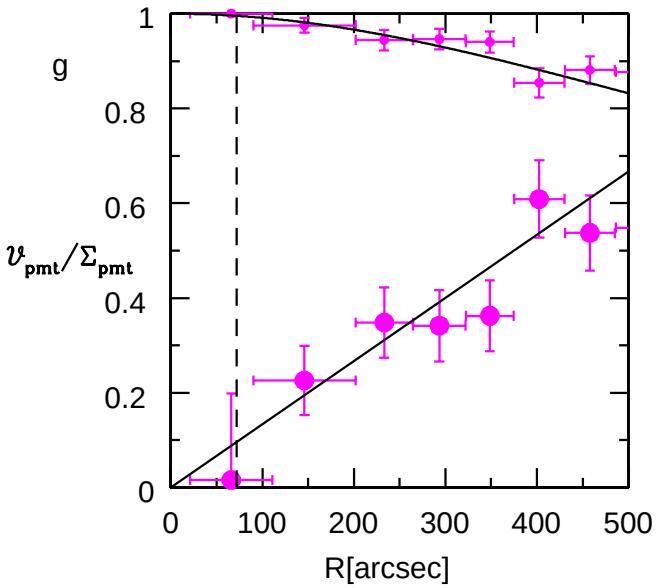

FIG. 4.— Observed ratios $\mathcal{V}_{\rm pmt}/\Sigma_{\rm pmt}$ (bottom; big dots; magenta in the on-line version) and $g \equiv \Sigma_{\rm pmt}/\bar{\Sigma}_{\rm pmt}$ (top; small dots; magenta), as function of projected radius R from the cluster center. The quantities in the nominator and denominator are all averages over an annulus, and are based on the data of vdV06. The solid lines indicate simple approximations to these quantities as described in the text. The dashed vertical line indicates the maximum radius for which we use HST proper motions from Paper I. The results shown here indicate that our inability to determine $\mathcal{V}_{\rm pmt}$ from the HST data does not prevent us from accurately determining the RMS motion $\bar{\Sigma}_{\rm pmt}$ in the tangential proper motion direction.

$\bar{\Sigma}_{\rm pmt}/\bar{\Sigma}_{\rm pmr} = 0.983 \pm 0.006$. Also, the data of vdV06 show that $V_{\rm los}/\sigma_{\rm los}$ is about a factor two lower than $\mathcal{V}_{\rm pmt}/\Sigma_{\rm pmt}$. Hence, the influence of rotation is even more negligible for the line-of-sight measurements at $R = 12''$ of NGB08 (see discussion in Section 5.1.1).

5.2.4. *Gauss-Hermite Moments*

To analyze the shapes of the HST proper motion distributions we binned the data in concentric circular annuli as in Section 5.2.2. For each bin we created separate histograms of the proper motions in the pmt and pmr directions. We used bins that correspond to $1\,\mathrm{km\,s^{-1}}$ for the canonical distance of ω Centauri ($D = 4.8$ kpc; vdV06). For each histogram we calculated the best-fitting Gaussian and the corresponding Gauss-Hermite moments, as in van der Marel et al. (2000). The odd moments are zero for distributions that are averaged over circles. Figure 5 shows the lowest order non-trivial even Gauss-Hermite moments h_4 and h_6. These were calculated for annuli that are $8''$ wide. The average values over all radii $R \leq 71.7''$ are $h_{4,\rm pmr} = -0.022 \pm 0.006$, $h_{4,\rm pmt} = -0.024 \pm 0.006$, $h_{6,\rm pmr} = -0.003 \pm 0.006$, $h_{6,\rm pmt} = 0.005 \pm 0.006$. The 8th and 10th order moments were also calculated, but are not shown here. They were found to be consistent with zero, like h_6. For all moments, the values for the pmr and pmt directions were found to be consistent within the errors. The only moment that is non-zero is h_4, with an average value over the two proper motion directions of $h_4 = -0.023 \pm 0.004$. This is indicative of proper motion distributions that are slightly more flat-topped than a Gaussian, and have slightly less extended wings. We will compare this to

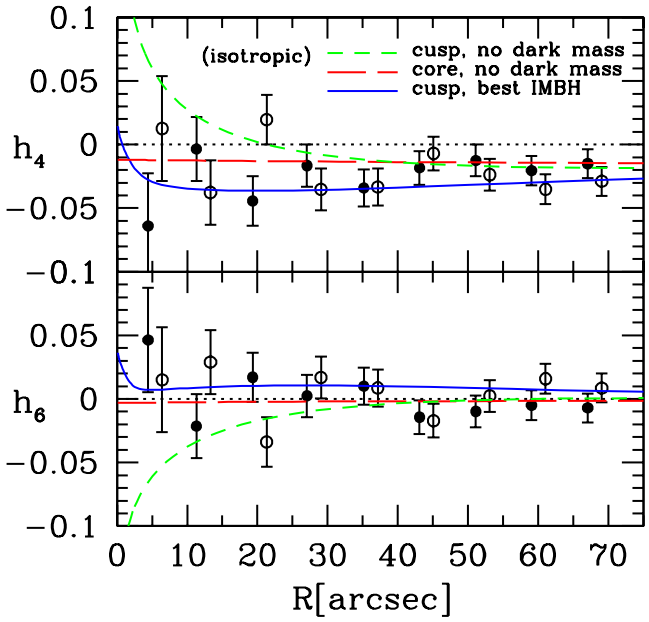

FIG. 5.— Lowest order even Gauss-Hermite moments h_4 (top) and h_6 (bottom) of the observed HST proper motion distributions as function of projected radius R from the cluster center. Different symbols indicate distributions in the pmr (solid dots) and pmt (open circles) directions. Data points in the two directions were slightly offset horizontally, for visual clarity. The Gauss-Hermite moments are not far from zero, indicating that the proper motion distributions are close to Gaussian. There are no systematic trends with radius. The curves show predictions of three isotropic models, as discussed in Section 6.7. The long-dashed curves (red in the online version) are for the isotropic core model with no dark mass. The solid curves (blue) are for the isotropic cusp model with its best-fit IMBH mass $M_{\rm BH} = 1.8 \times 10^4\ M_\odot$. Both of these models match the observed Gauss-Hermite moments to an average $|\Delta h_i| \lesssim 0.01$. The short-dashed curve (green) is for the isotropic cusp model with no dark mass. This model does not fit the observed Gauss-Hermite moments.

model predictions in Section 6.7.

6. DYNAMICAL DATA-MODEL COMPARISON

6.1. *Velocity Anisotropy*

The observed profile of $\bar{\Sigma}_{\rm pmt}/\bar{\Sigma}_{\rm pmr}$ shows statistically significant deviations from unity, both at small and at large radii (see Figure 3c). It is therefore important to allow for anisotropy in our models for ω Centauri.

To illustrate the relation between the model anisotropy function $\beta(r)$ and the observed quantity $\bar{\Sigma}_{\rm pmt}/\bar{\Sigma}_{\rm pmr}(R)$, we show in Figure 6a the predicted $\bar{\Sigma}_{\rm pmt}/\bar{\Sigma}_{\rm pmr}(R)$ for models with constant β as a function of radius r. Models were calculated with $(\overline{v_{\rm tan}^2}/\overline{v_r^2})^{1/2}$ ranging from 2/3 to 3/2, in equal logarithmic steps. At large radii, the proper motion anisotropy is a good tracer of the intrinsic anisotropy, consistent with the arguments presented in Section 2.7.3. For example, at $R = 10$ arcmin, $(\bar{\Sigma}_{\rm pmt}/\bar{\Sigma}_{\rm pmr}) - 1 = \tau[(\overline{v_{\rm tan}^2}/\overline{v_r^2})^{1/2} - 1]$, with $\tau = 0.7$–0.9 for the models calculated here, and $\tau \approx 0.8$ for $\beta \approx 0$. At small radii, the behavior of $\bar{\Sigma}_{\rm pmt}/\bar{\Sigma}_{\rm pmr}$ is a more complicated function of β. Tangentially anisotropic models ($\beta < 0$) all converge to $\bar{\Sigma}_{\rm pmt}/\bar{\Sigma}_{\rm pmr} = 1$ near the center, while radially anisotropic models ($0 < \beta \leq 1$) predict $\bar{\Sigma}_{\rm pmt}/\bar{\Sigma}_{\rm pmr} < 1$.

It is evident from Figure 6a that the observed $\bar{\Sigma}_{\rm pmt}/\bar{\Sigma}_{\rm pmr}(R)$ must tightly constrain the intrinsic $\beta(r)$. We fitted the combined kinematical data from Figure 3 with models that spanned a grid in β_0, β_∞ and r_a. The parameter β_0 determines the behavior of $\bar{\Sigma}_{\rm pmt}/\bar{\Sigma}_{\rm pmr}(R)$ near the center, β_∞ determines the behavior at large radii, and r_a is the transition radius. The minimum χ^2 was obtained for $\beta_0 = 0.13 \pm 0.02$, $\beta_\infty = -0.53 \pm 0.22$ and $\log r_a[{\rm arcsec}] = 2.86 \pm 0.12$. The error bars were obtained from the χ^2 contours of the fit.

The predicted $\bar{\Sigma}_{\rm pmt}/\bar{\Sigma}_{\rm pmr}(R)$ for the best-fit model is shown in Figure 6b. It provides an excellent fit. The predictions shown in the figure were calculated for core models with no dark mass. However, the predicted ratio $\bar{\Sigma}_{\rm pmt}/\bar{\Sigma}_{\rm pmr}(R)$ depends mostly on $\beta(r)$, and is virtually indistinguishable when considering instead models with a cusp or dark mass.

The error bars of the fit show that velocity anisotropy is detected at high statistical significance in ω Centauri. The parameters β_0 and β_∞ imply that the ratio $\overline{v_{\rm tan}^2}/\overline{v_r^2}$ transitions from 0.935 near the center to 1.235 at large radii. These are of course not necessarily the values at the very center and at infinity, since our model is constrained by proper motion data only over the range 1–1000 arcsec. Either way, there is a transition from radial anisotropy at small radii to tangential anisotropy at large radii. The parameter r_a indicates that the transition occurs at approximately 12 ± 3 arcmin (5 ± 1 core radii). This is broadly consistent with the modeling results of vdV06. They found (their Section 9.2) that ω Centauri is slightly radially anisotropic for $r \lesssim 10$ arcmin and that it becomes increasingly tangentially anisotropic outside this region.

The centers of globular clusters are generally believed to have isotropic velocity distributions because two-body relaxation tends to isotropize the orbits. However, ω Centauri has a long half-mass relaxation time of $\sim 10^{9.96\pm0.03}$ years (McLaughlin & van der Marel 2005). We showed in Paper I that mass segregation in the central region has not yet progressed to the point of energy equipartition. Since full energy equipartition has not yet been achieved, it is not surprising that complete velocity isotropy has not yet been achieved either.

A sufficient number of stars is necessary to measure the proper motion anisotropy with accuracy. Due to the finite number of stars at small radii, the anisotropy is not as well constrained at radii $R \lesssim 10''$ as it is further out. However, because Omega Cen has a very large core, most of the stars that are observed near the projected center are not actually close to the center in three dimensions (see, e.g., Section 6.1 of Paper I). One consequence of this is that the projected kinematics predicted near the center are influenced primarily by the anisotropy at larger radii. Changing the model anisotropy in the central $10''$ even quite substantially (e.g., $\pm 30\%$ in σ_r/σ_t) does not change the model predictions for the HST proper motion kinematics by more than a fraction of the error bars, even for the innermost data point. Therefore, uncertainties in anisotropy near the center do not significantly impact our predictions or conclusions.

6.2. *Cusp versus Core Models*

Figures 7a,b show the predicted and observed RMS projected velocities for the best-fit $\beta(r)$. Each panel of this figure shows the data for $\bar{\sigma}_{\rm los}(R)$ and $\bar{\sigma}_{\rm pm}(R)$ together in the same panel, with the observed proper

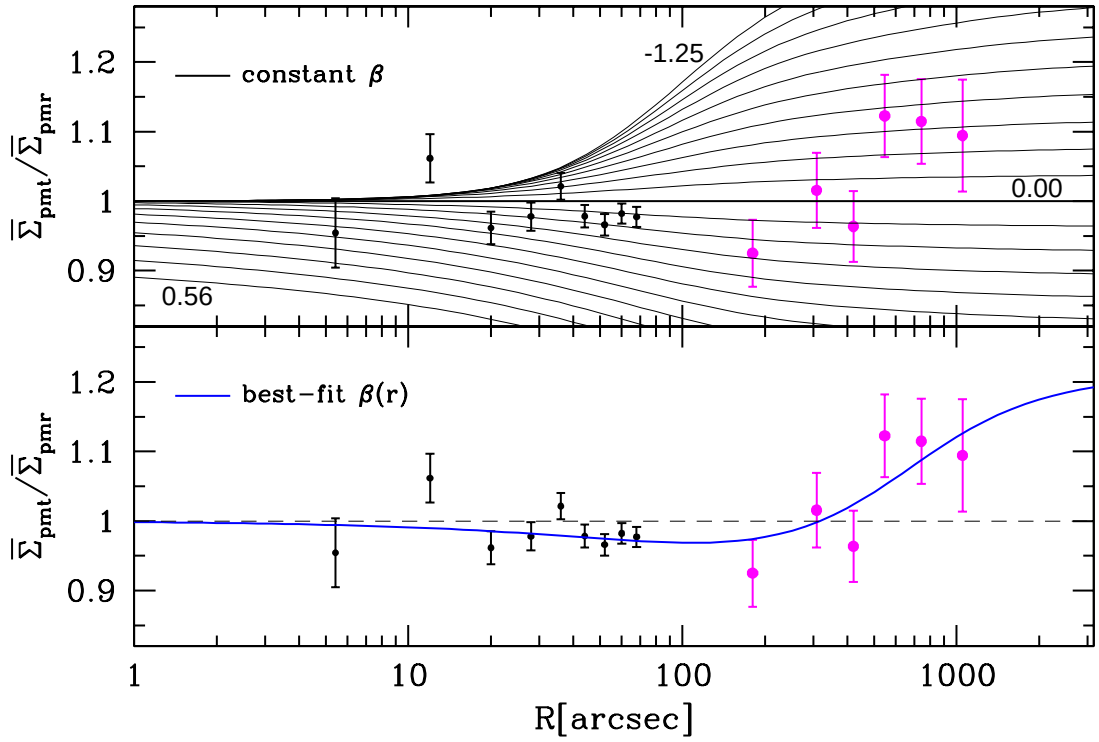

FIG. 6.— Dynamical data-model comparisons for the ratio $\bar{\Sigma}_{\rm pmt}/\bar{\Sigma}_{\rm pmr}$ as function of projected radius R from the cluster center. The data and the symbols are the same as in Figure 3c, and are the same in both panels. (a; top panel) Anisotropic models with constant β as function of radius. The models shown have $(\overline{v_{\rm tan}^2}/\overline{v_r^2})^{1/2}$ ranging from 2/3 to 3/2, in equal logarithmic steps. The corresponding β values are indicated for some of the curves. The horizontal line at $\bar{\Sigma}_{\rm pmt}/\bar{\Sigma}_{\rm pmr} = 1$ is for the isotropic model. Tangentially anisotropic models have higher $\bar{\Sigma}_{\rm pmt}/\bar{\Sigma}_{\rm pmr}$ than radially anisotropic models. The data are not well fit by models with constant β. (b) Anisotropic model with $\beta(r)$ in equation (15) chosen the optimize the fit to the data (blue in the on-line version). The model has $\beta_0 = 0.13$, $\beta_\infty = -0.53$ and $r_a = 729''$. The predictions in this figure were calculated for a core model with no dark mass. However, the predicted ratio $\bar{\Sigma}_{\rm pmt}/\bar{\Sigma}_{\rm pmr}(R)$ depends mostly on $\beta(r)$, and is virtually indistinguishable when considering instead models with a cusp or dark mass.

motions $\bar{\Sigma}_{\rm pm}(R)$ transformed to km/s using the best-fit distance implied by the model. For each model there are separate curves predicted for $\bar{\sigma}_{\rm los}(R)$ and $\bar{\sigma}_{\rm pm}(R)$ (dashed and solid curves, respectively), since these quantities are not the same in an anisotropic model. However, the difference is generally smaller than the observational error bars over the radial range where both types of data are available. There is no line-of-sight data available for $R \lesssim 10''$, so for visual clarity we do not show the predicted $\bar{\sigma}_{\rm los}(R)$ at those radii. At small radii $\bar{\sigma}_{\rm los}(R)$ exceeds $\bar{\sigma}_{\rm pm}(R)$ because of the model anisotropy, with $\bar{\sigma}_{\rm los} - \bar{\sigma}_{\rm pm} \approx 0.9\,{\rm km\,s^{-1}}$ at $R = 10''$ and $\bar{\sigma}_{\rm los} - \bar{\sigma}_{\rm pm} \approx 1.1\,{\rm km\,s^{-1}}$ at $R = 1''$.

Figure 7a shows the predictions for the core model fit to the projected intensity, and Figure 7b for the cusp model fit. The curves that predict the lowest $\bar{\sigma}$ at small radii (blue in the on-line version) are models with no dark mass. The core and cusp models generally predict the same dynamics at large radii, but differ slightly at small radii.

It is true in many analytical models with a cusped density profile and no central dark mass that the projected RMS velocity decreases towards the center (e.g., Tremaine et al. 1994). The same can be seen in Figure 7b for our model with $\gamma = 0.05$. Even though the cusp is quite shallow in projection, this corresponds to a much steeper three-dimensional luminosity density $j \propto r^{-1-\gamma}$ at asymptotically small radii. Similarly, the decrease in RMS velocities towards the center is much stronger intrinsically in three-dimensions than it is in projection. Either way, the observed RMS velocities do not show a significant dip near the center. In the absence of a dark mass, the core models therefore provide a better fit to the data than the cusp models.

The best fits without a dark mass have $\chi^2 = 235.3$ and 249.2 for the core and cusp models, respectively. There are 202 data points, yielding $N_{\rm DF} = 197$ degrees of freedom (there are five free parameters in the models when there is no dark mass). One expects $\chi \approx N_{\rm DF} \pm \sqrt{2N_{\rm DF}}$. The anisotropic core model is therefore consistent with the data at the 1.9σ level, while the cusp model is consistent at the 2.6σ level. These confidence levels assume that all data points in the fit are statistically independent, which is somewhat of a simplification. It is likely that samples from different line-of-sight velocity studies have some stars in common. However, this cannot be fully explored here since Scarpa et al. (2003) and Sollima et al. (2009) did not list individually which stars they observed.

Much of the excess $E(\chi^2) \equiv \chi^2 - N_{\rm DF} > 0$ for the fits is due to just two data points for $\bar{\sigma}_{\rm los}$ that appear anomalously high. The first "discrepant" data point is the measurement $\bar{\sigma}_{\rm los} = 23.0 \pm 2.0 {\rm km\,s^{-1}}$ at $R = 12.4''$ by NGB08. The second discrepant data point is the average $\bar{\sigma}_{\rm los} = 19.9 \pm 1.0\,{\rm km\,s^{-1}}$ for an annulus centered at $R = 46.0''$, obtained from the compiled data of vdV06. The former contributes 6.8 to the χ^2 of the fit for the core model, while the latter contributes 11.3. This adds up

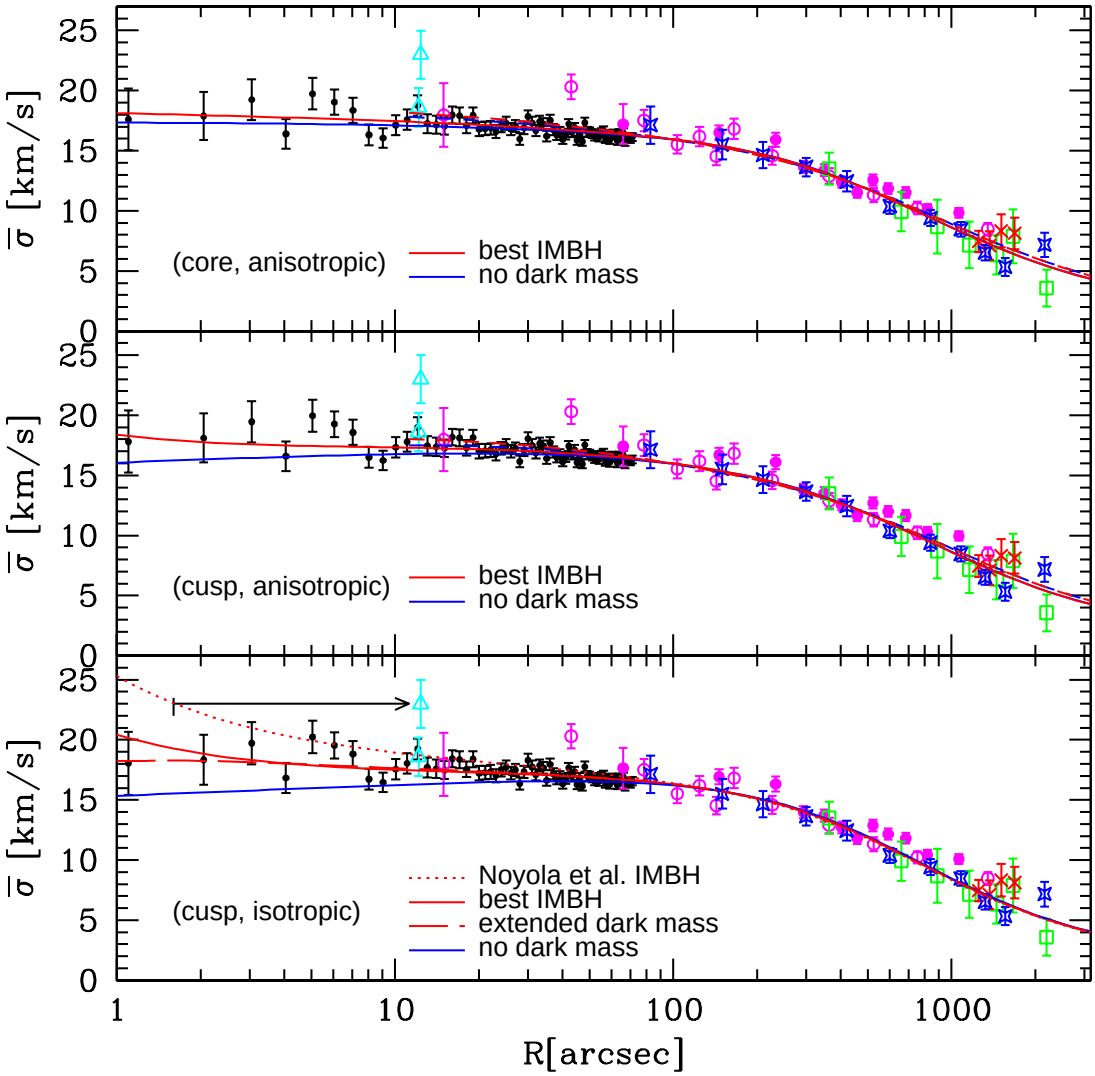

FIG. 7.— Dynamical data-model comparisons for the RMS projected velocity as function of projected radius R from the cluster center. The data and the symbols are the same as in Figure 3, and are the same in all panels. For plotting purposes, the proper motions $\bar{\Sigma}_{\rm pm}$ in mas/year were transformed to $\bar{\sigma}_{\rm pm}$ in km/s (solid symbols) using equation (25) with the best-fitting distance implied by the models. The arrow in the bottom panel indicates how one of the two data points from NGB08 moved due to our improved determination of the cluster center in Paper I. Curves are the predictions from various models. Solid curves are for $\bar{\sigma}_{\rm pm}$ and short-dashed curves are for $\bar{\sigma}_{\rm los}$. For visual clarity, $\bar{\sigma}_{\rm los}$ is not shown for $R \leq 10''$, where no $\bar{\sigma}_{\rm los}$ data are available. At larger radii, $\bar{\sigma}_{\rm pm}$ and $\bar{\sigma}_{\rm los}$ are quite similar, with differences becoming visual only at $R \gtrsim 1000''$. The curves that predict the lowest $\bar{\sigma}$ at small radii (blue in the on-line version) are models with no dark mass. The remaining curves (red) have some kind of dark mass in the center. (a; top panel) anisotropic models in which $\beta(r)$ was optimized to fit the data (see Figure 6), based on the core model for the projected intensity (see Figure 2). The top curve has the best-fit IMBH of mass $M_{\rm BH} = 4.1 \times 10^3\,M_\odot$. (b; middle panel) Anisotropic models similar to panel (a), but now based on the cusp model for the projected intensity (see Figure 2). The top curve has the best fit IMBH of mass $M_{\rm BH} = 8.7 \times 10^3\,M_\odot$. (c; bottom panel) Models similar to panel (b), but now for an isotropic velocity distribution (which does *not* fit the data for $\bar{\Sigma}_{\rm pmt}/\bar{\Sigma}_{\rm pmr}(R)$ in Figure 6). The quantities $\bar{\sigma}_{\rm los}$ and $\bar{\sigma}_{\rm pm}$ are the same for these isotropic models. The top three curves have different dark masses. The solid curve is for the best-fitting IMBH mass $M_{\rm BH} = 1.8 \times 10^4\,M_\odot$. The dotted curve is for the IMBH mass $M_{\rm BH} = 4.0 \times 10^4\,M_\odot$ advocated by NGB08. The long-dashed curve is for the best fitting dark cluster, which has $M_{\rm dark} = 2.0 \times 10^4\,M_\odot$ and $a_{\rm dark} = 3.0''$. It follows from analysis of the predictions in this figure, and in particular the top panel, that the presence of an IMBH in ω Centauri is not required, although IMBHs with masses $M_{\rm BH} \lesssim 1.2 \times 10^4\,M_\odot$ cannot be ruled out at $\sim 1\sigma$ confidence.

to 18.1, which is almost half of $E(\chi^2) = 38.3$.

The discrepant NGB08 data point pertains to similar radius as the other field that they observed, which is at $R = 12.1''$ from the cluster center (see Paper I). The measurement $\bar{\sigma}_{\rm los} = 18.6 \pm 1.6\,{\rm km\,s^{-1}}$ for that latter field is more consistent with the other measurements in our combined data set from Section 5. The two NGB08 measurements are inconsistent with each other at the 1.7σ level, despite the fact that that they pertain to the same radius, and despite the fact that the proper motions in these fields are consistent with each other (Paper I). We believe that this may be due to underestimates in the NGB08 error bars, since they did not explicitly include the contribution of shot noise (from the finite number of stars) to their error bars. Similarly, the measurement in the vdV06 annulus at $R = 46.0''$ appears inconsistent with other measurements in that same data set. The weighted average of the two adjacent annuli is lower and inconsistent with it at the 2.1σ level. This suggests that both discrepant measurements that contribute disproportionately to χ^2 may be spuriously high for unknown reasons.

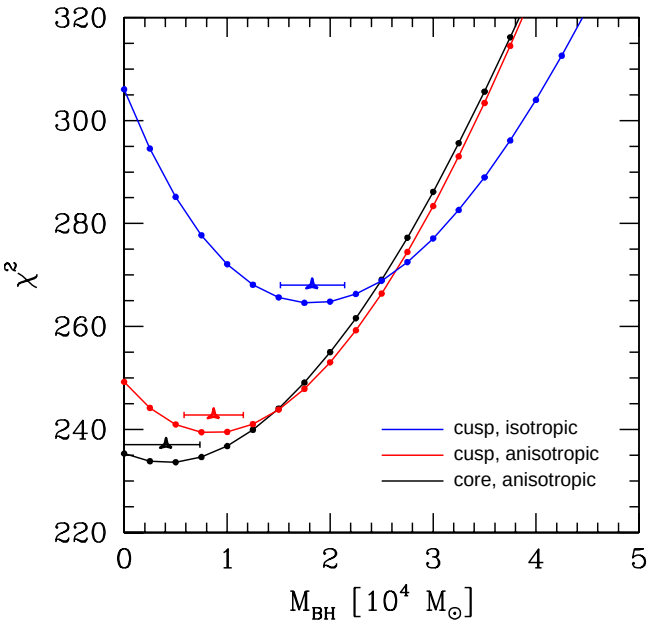

FIG. 8.— The χ^2 of the model fits to the kinematic data in Figure 3, as function of IMBH mass $M_{\rm BH}$. The resulting parabolae are, from bottom left to top right, respectively, obtained for the following models: anisotropic models with a core (black in the online version; see Figure 7a for actual model predictions); anisotropic models with a cusp (red; see Figure 7b); and isotropic models with a cusp (blue; see Figure 7c). Centered above the minimum of each parabola is a triangle with an associated error bar that indicates the best fit IMBH mass and its formal 1σ uncertainty. The anisotropic core models provide the overall best fits to the kinematics. The IMBH that optimizes the χ^2 for those models is not statistically significant. The small difference in χ^2 (vertical height) between the parabolae for the anisotropic core and cusp models is not a reason to prefer to core models over cusp models, in particular because the latter actually provide a somewhat better fit to the photometry (see discussion in the text).

Evidently, there are some internal discrepancies in the datasets themselves. Hence, the observed values of $E(\chi^2)$ should not be taken as a sign of shortcomings in the models. In fact, the values of $E(\chi^2)$ are remarkably low, given that we are fitting kinematical data compiled from 10 different original sources. Potential uncorrected systematics between different studies could easily have induced much larger data-model discrepancies.

One clear result from Figures 7a,b is that the data are well fit by the models out to the largest available radii. This contradicts arguments put forward by Scarpa et al. (2003) that the large radii kinematics of ω Centauri may be inconsistent with traditional theories of gravity. Our conclusion on this issue agrees with that of McLaughlin & Meylan (2003) and Sollima et al. (2009).

6.3. *IMBH*

To test for the presence of an IMBH we have also constructed models with $M_{\rm BH} > 0$ (and the same $\beta(r)$ profile). Models with no IMBH have one free parameter less than models with an IMBH. One would therefore on average expect them to fit worse by $\Delta\chi^2 = 1$. Moreover, random variations can add another $\Delta\chi^2 = 1$ (at 1σ confidence), even when the no-IMBH model is correct. Therefore, an IMBH is statistically significant in the model only if it improves the fit over a no-IMBH model by $\Delta\chi^2 \gtrsim 2$.

Figure 8 shows the curves of $\chi^2(M_{\rm BH})$ that quantify the quality of the fit. For the core model, the best-fit IMBH has mass $M_{\rm BH} = 4.1 \times 10^3\ M_\odot$. This improves the fit over the no-IMBH model by only $\Delta\chi^2 = 1.8$. This is not statistically significant. For the core model we can therefore determine only an upper limit to the mass of a possible IMBH, namely $M_{\rm BH} \leq 7.4 \times 10^3\ M_\odot$ at 1σ confidence. Figure 7a compares the best-fit core models with and without an IMBH. The inclusion of the IMBH makes very little difference to the predictions. The difference for the innermost data point at $R = 1.1''$ is only $0.8\,{\rm km\,s^{-1}}$, which is less than a quarter of the observational error bar at that radius.

For the cusp model, the inclusion of an IMBH improves the fit by $\Delta\chi^2 = 9.8$, which is significant at the 3.1σ level. The best-fit IMBH mass is $M_{\rm BH} = (8.7\pm2.9)\times10^3 M_\odot$ (with the error bar determined by the requirement $\Delta\chi^2 \leq 1$). Figure 7b compares the best-fit cusp models with and without an IMBH. The inclusion of the IMBH provides a small but visible improvement in the fit near the center. The reason that the IMBH is more massive and significant in the cusp model is due to the dip in RMS velocity predicted by these models when there is no dark mass.

In assessing the meaning of formal error bars on $M_{\rm BH}$, it is important to keep in mind what one may call "black hole bias". Statistical error bar estimates take into account only the random Gaussian uncertainties in the data. They do not take into account the systematic residuals that are inevitably present in any astronomical data-model comparison. In the present context these may include oversimplifications in the model assumptions (e.g., sphericity, equilibrium, the adopted density parameterization, no mass segregation among the luminous stars), the data reduction process (e.g., inability to measure absolute proper motion rotation), or the meaning of the data themselves (e.g., inability to separate orbital motion from potential binary motion). By adding $M_{\rm BH}$ as an extra free parameter to the fit, the model gains in ability to fit these systematic residuals that are not actually due to an IMBH. Because masses are positive definite ($M_{\rm BH} \geq 0$), this generally tends to bias in the direction of invoking more mass then there actually is, as compared to the opposite. Hence, $M_{\rm BH}$ tends to be biased high. Marginally significant non-zero $M_{\rm BH}$ values with no tell-tale signs of an IMBH (e.g., fast-moving stars or an $R^{-1/2}$ increase in $\bar\sigma$) may simply be indications of small systematic issues in the data-model comparison unrelated to an IMBH.

The core model with no IMBH fits the kinematical data a little better than the cusp model with an IMBH (see Figure 8). The difference is $\Delta\chi^2 = 4.0$, which is nominally significant at the 2.0σ level. However, as discussed in Section 4, the cusp model nominally provides a better fit to the photometric data. The difference for a generalized nuker fit is $\Delta\chi^2 = 6.8$, which is nominally significant at the 2.6σ level. One could in principle construct a grand-total $\Delta\chi^2$ that sums the photometric and kinematic values. However, we have not done this here. The arguments about whether a core or cusp model better fits the photometry are complex (see Section 4). They are not easily captured in a single number without having to make arbitrary choices about, e.g., what radii to include in the comparison. Either way, when comparing

both the photometric and kinematic information for the core and cusp models we feel that there is no sound statistical basis to prefer one model over the other. In view of this, we conclude that the existing data do not imply that an IMBH is present in ω Centauri. However, IMBHs with masses $M_{\rm BH} \lesssim 1.2 \times 10^4\,M_\odot$ cannot be ruled out at 1σ confidence (or $\lesssim 1.8 \times 10^4\,M_\odot$ at 3σ confidence).

6.4. *Distance and Mass-to-Light Ratio*

The best-fit distance and mass-to-light ratio depend only slightly on the particular model we adopt. The core model without a dark mass has $D = 4.70 \pm 0.06$ kpc and $\Upsilon_V = 2.64 \pm 0.03$ (here and henceforth, mass-to-light ratios are given in V-band solar units). The cusp model with an IMBH has $D = 4.75 \pm 0.06$ kpc and $\Upsilon_V = 2.59 \pm 0.03$.

Our results for D and Υ_V are entirely consistent with those inferred by vdV06 from fitting only ground-based projected intensity and kinematical data. They found that $D = 4.8 \pm 0.3$ kpc and $\Upsilon_V = 2.5 \pm 0.1$. Their modeling technique was considerably more sophisticated than ours, allowing for axisymmetry, inclination, ellipticity variations with radius, and arbitrary profiles of rotation and velocity-dispersion anisotropy. The reason that our error bars are smaller than theirs is likely a combination of two effects. First, we have considerably more data at our disposal than did vdV06, and in particular we have a factor ~ 11 more stars with measured proper motions. This produces a significant decrease in the random uncertainties. But second, in our simpler models we cannot explore the full variety of phase-space distributions that might fit the data with non-standard distances or mass-to-light ratios. Therefore, we are not quantifying systematic errors as rigorously as vdV06, and as a result our errors are artificially lowered compared to theirs.

The fact that our D and Υ_V agree with those of vdV06 indicates that there is no reason to mistrust that our spherical models can address the central mass distribution of ω Centauri with credible accuracy. This is further supported by the facts that both the elongation (Geyer, Nelles, & Hopp 1983) and the rotation rate (Section 5.2.3) decrease towards the cluster center. To get good results we did have to make sure to model RMS velocities (which sum rotation velocities and velocity dispersions in quadrature) and not merely velocity dispersions. Also, one should fit only quantities that are properly averaged over annuli on the projected plane of the sky. If these things are not done, then biased estimates are obtained for D and Υ_V, as demonstrated in Appendix C of vdV06.

6.5. *Isotropic Models*

Isotropic models predict that $\bar\Sigma_{\rm pmt}/\bar\Sigma_{\rm pmr} = 1$ at all radii, so they are not generally appropriate for ω Centauri. However, isotropic models have the advantage that the full velocity distributions $\mathcal{L}_{\rm iso}(v,R)$ can be calculated as described in Section 2.5. Also, isotropic models are often used for globular clusters, so it is useful to understand how the predictions of such models deviate from more general anisotropic models.

Figure 8 shows the curve of $\chi^2(M_{\rm BH})$ for isotropic models with an IMBH. The models fit significantly worse than the anisotropic models, as shown by the higher χ^2. Within the realm of isotropic models, the best fit is provided by $M_{\rm BH} = (1.8 \pm 0.3) \times 10^4\,M_\odot$. This model has $D = 4.81 \pm 0.06$ kpc and $\Upsilon_V = 2.61 \pm 0.03$. Figure 7c shows the data-model comparison for the isotropic model with this IMBH. We also show the predictions for $M_{\rm BH} = 0$, as well as for the value $M_{\rm BH} = 4.0 \times 10^4\,M_\odot$ advocated by NGB08.

The NGB08 IMBH mass was based on their measurement of $\bar\sigma_{\rm los} = 23.0 \pm 2.0\,{\rm km\,s^{-1}}$ at a position they believed to be the cluster center. This high IMBH mass is now clearly ruled out, even for an isotropic model, for two reasons. First, Paper I showed that this measurement actually applies to a larger distance $R = 12.4''$ from the cluster center. The arrow in Figure 7c demonstrates how this moved the corresponding line-of-sight velocity measurement. And second, the high measured RMS velocity was not confirmed by proper motion measurements, either at the same position or on the actual cluster center. Note in Figure 7c that the isotropic model with the NGB08 IMBH does appear to match well the data at $R = 5$–$7''$. However, it overpredicts the data at both $R \le 4''$ and $R = 8$–$10''$. Since all data points were derived in the same manner and are equally valid, there is no reason attribute more weight to the data at $R = 5$–$7''$. In particular, the data at $R \le 4''$ contain most of the information on the very central mass distribution, and they clearly rule out an IMBH mass as high as advocated by NGB08 (independent of the model anisotropy near the center).

It is evident from Figure 8 that isotropic models require a higher IMBH mass than the best-fit anisotropic models. This is not generally true for isotropic models, but is a specific consequence of the fact that ω Centauri is radially anisotropic near the center and tangentially anisotropic at large radii. This affects the general gradient in RMS velocity from small to large radii (see e.g., Figures 10 and 11 of van der Marel 1994). The anisotropic model without a dark mass has a steeper gradient towards the center than the corresponding isotropic model. The anisotropic model therefore requires less dark mass to fit the observed gradient. This indicates that one should be careful in application of isotropic models to studies of IMBHs. Depending on the exact anisotropy of the cluster, the assumption of isotropy can lead to either an overestimated or an underestimated IMBH mass, or it can require an IMBH when none is present.

6.6. *Dark cluster*

When a dark mass is clearly required by the data, as in the case of isotropic models with a cusp, one can ask whether an extended dark cluster may provide a better fit than an IMBH. Figure 9 shows a two-dimensional contour plot of $\Delta\chi^2$ in the parameter space of $(a_{\rm dark}, M_{\rm dark})$ for the isotropic cusp model. The best fit is obtained for $M_{\rm dark} = 2.0 \times 10^4\,M_\odot$ and $a_{\rm dark} = 3''$. The predictions of this model are shown in Figure 7c. It has a somewhat shallower increase in RMS velocity towards the center than the IMBH model. The dark-cluster model makes an improvement of only $\Delta\chi^2 = 1.7$ over the IMBH model, while increasing the number of free parameters by one. This is not statistically significant. Therefore, one can interpret Figure 9 to mean that if there is a dark mass in ω Centauri, then its extent must be $\lesssim 7''$ at 1σ confidence.

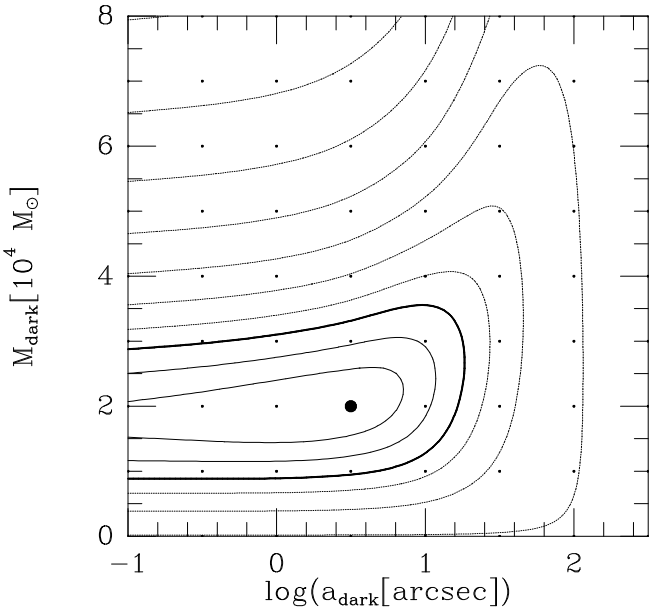

FIG. 9.— Contours of $\Delta\chi^2$ in the two-dimensional plane of $(a_{\rm dark}, M_{\rm dark})$ for the fit of isotropic cusp models to the data in Figure 3. The distance D and mass-to-light ratio Υ_V were optimized separately at each $(a_{\rm dark}, M_{\rm dark})$ for which a model was calculated (indicated with small dots). The model for which the minimum χ^2 was obtained is indicated by the big dot. The first three contours (solid) around the minimum correspond to 1σ, 2σ, and 3σ (bold) confidence contours, respectively. Each subsequent contour (dashed) increases $\Delta\chi^2$ by a constant factor. Models with a central dark points mass (an IMBH; i.e., $a_{\rm dark} = 0$) are shown on the vertical axis on the left. Models with no central dark mass lie on the horizontal axis on the bottom. If there is a dark mass in ω Centauri (as must be the case in isotropic models, but these do *not* fit the data for $\bar{\Sigma}_{\rm pmt}/\bar{\Sigma}_{\rm pmr}(R)$ in Figure 6) then its extent must be $\lesssim 7''$ at 1σ confidence.

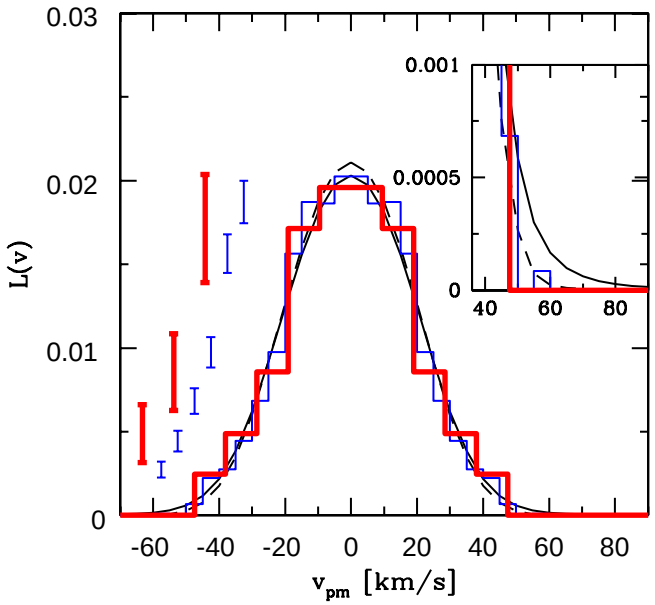

FIG. 10.— Symmetrized histograms of the observed proper motion velocities for apertures of radii $R = 3'$ (bold; red in the on-line version) and $R = 10'$ (thin; blue), respectively. Proper motions in both the pmr and pmt directions are included. They were transformed to physical units of km/s using the best-fit model distance. Typical error bars are shown on the left; they were offset horizontally from the histograms for visual clarity. The predictions for the isotropic cusp model with the best fit IMBH mass $M_{\rm BH} = 1.8 \times 10^4\ M_\odot$ are over-plotted as curves (solid for the $R = 3'$ aperture, and dashed for the $R = 10'$ aperture). The inset on the right shows a blow-up of the profile wings on an expanded vertical scale. The models predict broader wings than observed, but the difference is not statistically significant (as discussed in the text). This is because the total area under the model curves beyond 60 km s^{-1} corresponds to less than 1 predicted star.

The central density of the best-fitting dark cluster is $\rho_{0,\rm dark} \equiv M_{\rm dark}/(4\pi a_{\rm dark}^3/3)$, according to equation (7). Using equation (4) to transform angular units to physical units, this yields for the core model $\rho_{0,\rm dark} = 1.4 \times 10^7\ M_\odot\ {\rm pc}^{-3}$. The central density of luminous matter in this model is only $\rho_{0,\rm lum} = 3.3 \times 10^3\ M_\odot\ {\rm pc}^{-3}$. This implies a central $M/L = \Upsilon_V[1 + (\rho_{0,\rm dark}/\rho_{0,\rm lum})] = 1.1 \times 10^4$. This applies to an isotropic model with $M_{\rm dark} = 2.0 \times 10^4\ M_\odot$. For an anisotropic model with a lower $M_{\rm dark}$, the required M/L scales approximately linearly with $M_{\rm dark}$. The (maximum) size $a_{\rm dark}$ of the dark mass fit is relatively insensitive to the exact anisotropy. Either way, if ω Centauri does indeed have a dark central cluster, this would be indicative of quite an extreme amount of mass segregation or a very top-heavy initial mass function. If a dark mass is invoked to explain the data, then an IMBH may be easier to explain than such a concentrated dark cluster.

6.7. *Velocity Distribution Shapes*

For our isotropic models we calculated the projected velocity distributions $\mathcal{L}_{\rm iso}(v, R)$ as described in Section 2.5, and from this the Gauss-Hermite moments $h_{i,\rm iso}(R)$. We did not take the effect of observational proper motion uncertainties into account in the models (essentially a convolution of the model predictions with the error distribution). This has negligible effect on the Gauss-Hermite moments because the observational errors are much less than the intrinsic cluster dispersion. The curves over-plotted in Figure 5 show the model predictions for three models: the isotropic core model with no dark mass, the isotropic cusp model with its best-fit $M_{\rm BH} = 1.8 \times 10^4\ M_\odot$, and the isotropic cusp model with no dark mass.

The core model with no dark mass and the cusp model with an IMBH both fit the observed Gauss-Hermite moments within the error bars. Over the range $5'' \lesssim R \lesssim 71.7''$, the predicted Gauss-Hermite moments for these models are approximately constant. For the core model without dark mass they are $h_{4,\rm iso}(R) \approx -0.013$ and $h_{6,\rm iso}(R) \approx -0.002$, and for the cusp model with an IMBH they are $h_{4,\rm iso}(R) \approx -0.034$ and $h_{6,\rm iso}(R) \approx 0.009$. These averages do deviate in statistically significant manner from the observed averages, $h_4 = -0.023 \pm 0.004$ and $h_6 = 0.001 \pm 0.004$ (see Section 5.2.4). This is not surprising, given that we have already established that ω Centauri does not have an isotropic velocity distribution, not even near its center. However, the differences between the predicted and the average observed Gauss-Hermite moments are quite small $|\Delta h_i| \lesssim 0.01$. For comparison, models that range in anisotropy from fully tangential to fully radial can easily span the range $\Delta h_i \approx \pm 0.2$ (e.g., van der Marel & Franx 1993). The measured Gauss-Hermite moments are therefore consistent with the fact that the velocity distribution is not far from isotropic near the center of ω Centauri.

The cusp model without dark mass does *not* fit the observed Gauss-Hermite moments. As discussed in Sec-

tion 6.2, this model has a strong decrease in its intrinsic (unprojected) RMS velocity towards the center. The decrease in the projected RMS velocity is relatively mild, as shown in Figure 7c. However, there is a strong gradient in the RMS velocity along the line of sight. This leads to strongly non-Gaussian velocity distributions. In a central aperture of $R = 8''$ radius, as used for the innermost observational data point in Figure 5, the predictions are $h_{4,\rm iso} = 0.063$ and $h_{6,\rm iso} = -0.063$. This deviates for each order by $\sim 3\sigma$ from the observed values $h_4 = -0.026 \pm 0.029$ and $h_6 = 0.031 \pm 0.029$ (averaged over the pmr and pmt directions). While this result was derived for isotropic models, the large predicted deviations from Gaussian velocity distributions are likely generic, and would exist in anisotropic models as well. So if ω Centauri has a central cusp in its projected intensity profile, then the observed velocity distributions rule out models without a dark mass. Of course, Figure 7b,c show that such models also do not provide good fits to the projected profiles of RMS velocity.

Figure 5 shows that an isotropic model *with* an IMBH predicts increased h_4 and h_6 in the central $R \lesssim 5''$, corresponding to profiles with broader wings than a Gaussian. To do a more detailed data-model comparison for the wings we show in Figure 10 the histograms of the observed proper motions for apertures of radii $R = 3''$ and $R = 10''$. These apertures contain $N = 43$ and $N = 585$ stars with well-measured proper motions, respectively. The proper motion coordinates in the pmr and pmt direction were both included in each histogram, as appropriate for an isotropic velocity distribution. The histograms were symmetrized to decrease the uncertainties. The predictions for the isotropic cusp model with $M_{\rm BH} = 1.8 \times 10^4\,M_\odot$ are over-plotted as curves. The predicted velocity distribution for the $R = 3''$ aperture has more extended wings than the observed histogram. The wings are much reduced in the predicted velocity distribution for the $R = 10''$ aperture. This is because none of the added stars at $3'' < R \leq 10''$ are close to the black hole, so they do not move at unusually high velocities.

The observed histograms do not extend beyond $60\,{\rm km\,s^{-1}}$. The maximum observed value of either $|v_{\rm pmt}|$ or $|v_{\rm pmr}|$ inside $R = 10''$ is $59.4\,{\rm km\,s^{-1}}$. No stars were rejected as non cluster members inside this radius because of their fast motion (see Section 5.2.1). To assess whether these observations are statistically consistent with the wings of the predicted distributions, let f be the fraction of the normalized model distribution at $|v| > 60\,{\rm km\,s^{-1}}$. According to the models, this is $f = 3.8 \times 10^{-3}$ for the $R = 3''$ aperture and $f = 3.9 \times 10^{-4}$ for the $R = 10''$ aperture. The expectation value for the number of stars with a velocity component at $|v| > 60\,{\rm km\,s^{-1}}$ is $E = 2Nf$. The probability that all of the $2N$ measured velocities have $|v| \leq 60\,{\rm km\,s^{-1}}$ is $P = (1-f)^{2N}$. This yields for the $R = 3''$ aperture that $E = 0.32$ and $P = 0.72$, while for the $R = 10''$ aperture $E = 0.46$ and $P = 0.63$.

Since less than a single fast-moving star was predicted, the fact none were observed is not statistically inconsistent with the models. This does not change when we use larger apertures, since the models do not predict any fast-moving stars outside $R = 10''$. It also does not change by using smaller apertures, since in that case the sample of observed stars becomes very small. Therefore, the absence of fast-moving stars in the data cannot be used to independently rule out the presence of an IMBH with mass $M_{\rm BH} = 1.8 \times 10^4\,M_\odot$. To increase the predicted number of fast-moving stars one would need to increase the number of stars with measured proper motions, i.e., extend the kinematical observations to fainter magnitudes. We have experimented with looser cuts on our proper motion catalog. This allows us to increase the sample size by a factor ~ 2 (see Paper I). In this extended catalog there is no star with a proper motion coordinate in excess of $65\,{\rm km\,s^{-1}}$ within $R = 10''$. This provides somewhat tighter constraints on the presence of an IMBH, with the quoted values of P roughly decreasing to their squared values. Even then, it is still not possible to rule out an IMBH of mass $M_{\rm BH} = 1.8 \times 10^4\,M_\odot$ with reasonable confidence.

Alternatively, E increases and P decreases when the BH mass is increased. For the IMBH of mass $M_{\rm BH} = 4.0 \times 10^4\,M_\odot$ suggested by NGB08, and sticking as before with our high-quality proper motion catalog of Section 5.2.1, we obtain $E = 2.9$ and $P = 0.05$ for the aperture with $R = 10''$. This implies that the absence of fast-moving stars rules out all IMBHs with $M_{\rm BH} \gtrsim 4.0 \times 10^4 M_\odot$ at 95% confidence. This result is not very competitive for ω Centauri, since we already know from modeling of the RMS velocities that any IMBH must have a mass at least 3.3 times lower than this anyway. However, this method has the advantage that it does not require any accurate measurement of RMS velocities. It may therefore be useful for other clusters, in cases when the observational errors may be too large for accurate measurement of the RMS velocity profile.

6.8. *Brownian Motion*

We have assumed in the modeling that any IMBH must reside at the cluster center. In reality, an IMBH would exhibit Brownian motion as a result of its energy equipartition with surrounding stars. Chatterjee, Hernquist & Loeb (2002) derived for the one-dimensional RMS offset from the cluster center that

$$x_{\rm RMS} = (2\tilde{m}/9M_{\rm BH})^{1/2}\,r_0. \qquad (34)$$

This was derived for an analytical Plummer model with core radius r_0, which provides a reasonable description of (non core-collapsed) globular clusters. Chatterjee et al. considered single-mass models with stars of mass $\tilde{m}$. However, their results should be valid for multi-mass models as well, provided that the quantity $\tilde{m} \equiv \langle m^2 \rangle / \langle m \rangle$ is defined appropriately in terms of averages over the stellar mass function (Merritt, Berczik & Laun 2007).

We take for r_0 the King core radius of $141''$ (McLaughlin & van der Marel 2005) and for $M_{\rm BH}$ the upper limit of $1.2 \times 10^4\,M_\odot$ derived in Section 6.3. For a Salpeter mass function from 0.1–10 $M_\odot$, $\tilde{m} = 1.27\,M_\odot$. We then obtain $x_{\rm RMS} = 0.69''$. This is significantly less than the $1.55''$ radius of the smallest aperture used in the kinematical analysis (see Section 5.2.2). Therefore, the expected Brownian motion of an IMBH should not affect significantly the analysis that we have presented here.

IMBHs with larger masses than those considered here, placed at considerable offsets from the cluster center (consistent with their expected Brownian motion), might

TABLE 1
Globular clusters with IMBH constraints

cluster	D (kpc)	V_0 (mag)	M/L_V ($\odot$)	$M_{\rm tot}$ ($M_\odot$)	$\sigma_{\rm e}$ (km/s)	$M_{\rm BH}$[Tre] ($M_\odot$)	$M_{\rm BH}$[obs] ($M_\odot$)	data	$M_{\rm BH}$[obs] / $M_{\rm tot}$
(1)	(2)	(3)	(4)	(5)	(6)	(7)	(8)	(9)	(10)
47 Tuc	4.5^b	3.91^b	2.4^b	1.1×10^6	9.8^k	7.3×10^2	$<1.5\times10^{3\,g}$	discrete PM	$<0.13\%$
Omega Cen	4.7^a	3.14^b	2.6^a	2.8×10^6	15.7^j	4.8×10^3	$<1.2\times10^{4\,a}$	discrete PM+LOS	$<0.43\%$
M15	10.3^l	5.89^e	1.6^c	6.2×10^5	12.1^c	1.7×10^3	$<4.4\times10^{3\,h}$	discrete PM+LOS	$<0.71\%$
NGC 2298	10.7^b	9.36^b	1.9^b	3.4×10^4	2.4^k	2.6×10^0	$<3.4\times10^{2\,f}$	mass segregation	$<1.0\%$
G1	770^i	13.49^i	2.8^d	5.7×10^6	25.1^i	3.2×10^4	$(1.8\pm0.5)\times10^{4\,d}$	unresolved LOS	$(0.32\pm0.09)\%$

Note. — Column (1) lists the cluster name. Column (2) lists the cluster distance D. Column (3) lists the extinction-corrected total apparent magnitude V_0. Column (4) lists the V-band mass-to-light ratio M/L_V in units of $M_\odot/L_{\odot\,V}$. Column (5) lists the total cluster mass $M_{\rm tot}$ derived from columns (2)–(4). Column (6) lists the effective velocity dispersion $\sigma_{\rm e}$. Column (7) lists the value of $M_{\rm BH}$ predicted by the $M_{\rm BH}$ vs. σ_e relationship for galaxies of Tremaine et al. (2002), using the value of $\sigma_{\rm e}$ in column (6). The uncertainty in the predicted $M_{\rm BH}$ due to the uncertainties in the relation itself is a factor ~ 1.5. There is also intrinsic scatter about the relationship of a factor ~ 2. Column (8) lists the observational constraint on the mass $M_{\rm BH}$ of any IMBH. Column (9) lists the type of data on which the observational constraint in column (8) is based. This can be either discrete velocities in the proper motion (PM) and/or line-of-sight (LOS) directions; unresolved observations of line-of-sight kinematics; or measurements of the amount of mass segregation, which can be compared to model predictions. Column (10) lists the observational constraint on the ratio $M_{\rm BH}/M_{\rm tot}$. Sources of the numbers in the table are: [a] This paper. [b] McLaughlin & van der Marel (2005). [c] Gerssen et al. (2002). [d] Gebhardt et al. (2005). [e] Harris (1996). [f] Pasquato et al. (2009). [g] McLaughlin et al. (2006). [h] Gerssen et al. (2003). [i] Meylan et al. (2001). [j] Line-of-sight velocity dispersion in an aperture of size equal to the effective radius, calculated from the models in this paper; this is 85% of the central value. [k] The central model velocity dispersion value in McLaughlin & van der Marel (2005), multiplied by the same 85% correction derived in footnote j. [l] van den Bosch et al. (2006).

have gone unnoticed in our analysis. However, there is no independent motivation to consider such a situation. In Paper I we showed that the kinematical center of stars in ω Centauri agrees with the star count center to within its $\sim 2''$ uncertainty.

7. GLOBULAR CLUSTER IMBH DEMOGRAPHICS

The self-gravity of a cluster gives it a negative heat capacity that makes it vulnerable to the so-called "gravothermal catastrophe". This makes the core collapse on a timescale proportional to the half-mass relaxation time. This is normally halted by formation and/or heating of binaries. However, the most massive stars in a cluster tend to undergo core collapse more or less independently of the other cluster stars on a timescale that is less than the core collapse time for the cluster as a whole. If this happens faster than the main sequence evolution time of these stars (i.e., before they become compact remnants), then they will undergo physical collisions that lead to the formation of a single Very Massive Star (VMS). Such a VMS could plausibly evolve into an IMBH.

Portegies Zwart & McMillan (2002) proposed the aforementioned scenario and performed N-body simulations to show that a VMS might grow to $M_{\rm VMS}/M_{\rm tot}\approx 0.1\%$, with $M_{\rm tot}$ being the total cluster mass. Gurkan et al. (2004) and Freitag et al. (2006) used Monte-Carlo simulations with prescriptions and models for stellar collisions and found that the resulting VMS could even grow up to $M_{\rm VMS}/M_{\rm tot}\approx 1\%$. However, it is not clear what the resulting IMBH mass might be. The evolution of a VMS may yield significant mass loss before the final collapse. Also, a VMS will only form through this scenario in clusters with very short initial half-mass relaxation times, $\lesssim 30$ Myr. Some star clusters (e.g., the Arches cluster) are known to have such short relaxation times. However, most globular clusters have much longer current relaxation times, although it is not straightforward to estimate what their relaxation time at birth may have been (Ardi et al. 2008).

Alternative scenarios for IMBH formation in globular clusters have been proposed as well (see e.g. the review in van der Marel 2004). This includes the merging of stellar-mass black holes. O'Leary et al. (2006) found that this may lead to growth up to $M_{\rm IMBH}/M_{\rm tot}\approx 0.1\%$. Whether this indeed happens depends on the typical BH merger recoil speed. Significant recoils will kick black holes out of the cluster before they have a chance to grow.

Overall, the predictions for IMBH formation in globular clusters have significant uncertainties. Observations will therefore need to be the primary guide for the study of IMBH demographics in globular clusters. For ω Centauri one may combine the distance and mass-to-light ratio derived in Section 6.4 with the extinction-corrected total V-band magnitude to determine that $M_{\rm tot}=2.8\times10^6\,M_\odot$. The IMBH mass upper limit from Section 6.3 therefore corresponds to $M_{\rm BH}/M_{\rm tot}\lesssim 0.43\%$. Table 1 lists the corresponding constraints for the other globular clusters that have been well-studied dynamically, as discussed in Section 1. We also include the limit recently reported by Pasquato et al. (2009) based on a study of the observed mass segregation in the cluster NGC 2298. An IMBH is expected to reduce the amount of mass-segregation that is otherwise expected in a well-relaxed cluster. The suggested IMBH in G1 weighs in at $M_{\rm BH}/M_{\rm tot}=(0.32\pm0.09)\%$. The four other clusters in the table only provide upper limits in the range 0.1–1%. Therefore, the data allow us to probe in a mass range that is of interest in view of existing theories.

The IMBHs suspected in some globular clusters may have been similar to the initial seeds that grew to super-

massive black holes (SMBHs) in the centers of galaxies. It is therefore of interest to compare the results in Table 1 to what is known about SMBHs. The masses of SMBHs scale with either the galaxy bulge mass $M_{\rm bul}$, or alternatively, with the fourth power of the velocity dispersion σ. Haering & Rix (2004) found that $M_{\rm BH}/M_{\rm bul} \approx 0.14 \pm 0.04\%$. This is below where it has been possible to probe for most globular clusters. Only for 47 Tuc is there a limit $M_{\rm BH}/M_{\rm tot} \lesssim 0.13\%$ (McLaughlin et al. 2006). Tremaine et al. (2002) discussed the $M_{\rm BH}$–σ relation proposed for SMBHs. In Table 1 we list for each cluster the value of $M_{\rm BH}$ predicted by their relation. All of the available $M_{\rm BH}$ upper limits are at least a factor of 2 above these predictions. Therefore, the data are insufficient to confirm or rule out the hypothesis that globular clusters generally have IMBHs that follow the same relations as established for SMBHs. However, for the case of G1 the suggested IMBH mass does seem reasonably consistent with these relations (Gebhardt et al. 2005).

8. DISCUSSION AND CONCLUSIONS

We have presented a detailed dynamical analysis of the star-count, surface-brightness, and kinematical data available for ω Centauri, with a particular focus on the new HST data presented in Paper I. Based on the observed profile of the projected density, our models use the Jeans equation to yield predictions for the projected profiles of RMS line-of-sight velocity $\bar\sigma$ or proper motion $\bar\Sigma$ as function of projected distance R from the cluster center, in each of the three orthogonal coordinate directions (line of sight, proper motion radial, and proper motion tangential). We do not include the effect of mass segregation on the model predictions at large radii, but we do take into account the observed (partial) energy equipartition between stars of different masses. The predictions are compared in a χ^2 sense to observations, to infer the best-fit values of the model parameters and their error bars.

The model parameters are uniquely determined by the data. The profile $\beta(r)$ of the intrinsic velocity anisotropy is tightly constrained by the observed profile $[\bar\Sigma_{\rm pmt}/\bar\Sigma_{\rm pmr}](R)$. The models are therefore unaffected by the mass-anisotropy degeneracy that often plagues line-of-sight velocity studies. The mass-to-light ratio Υ of the stellar population is fixed by normalization of the observed $\bar\sigma_{\rm los}(R)$ and $\bar\Sigma_{\rm pm}(R)$ at large radii. The distance D is set by comparison of the observed $\bar\Sigma_{\rm pm}(R)$ in mas/yr to the predicted $\bar\sigma_{\rm pm}(r)$ in km/s. And the presence and properties of any dark mass in the center, such as an IMBH or dark cluster, are constrained by the behaviors of $\bar\sigma_{\rm los}(R)$ and $\bar\Sigma_{\rm pm}(R)$ at small radii.

The new HST proper motion data provide a significant improvement in our ability to constrain the dynamical models of ω Centauri, as compared to previous modeling efforts (e.g., vdV06; NGB08). The HST sample increases the number of stars with one or more accurately measured velocity components by about an order of magnitude. This allows for the first time the measurement of velocity dispersions at $R \lesssim 10''$. We have derived kinematical profiles down to $R \approx 1''$, at which point there cease to be enough stars with measured proper motions to accurately measure a dispersion. The profile of $\bar\Sigma_{\rm pm}(R)$ is consistent with being flat in the central $R \lesssim 15''$. The absence of an increase in RMS stellar velocities towards the center provides strong constraints on the possible presence of any dark mass.

The HST star count data from Paper I provide an upper limit $\gamma \lesssim 0.07$ to the central logarithmic cusp of slope of the projected density profile. The innermost data points are well matched by previously published King and Wilson models with a flat core. A generalized nuker profile fits best at all cluster radii when a shallow cusp is invoked, but this overpredicts the innermost datapoints at $R \lesssim 4''$. Dynamical model predictions depend sensitively on whether or not there is a density cusp, so in our analysis we considered separately models with a core ($\gamma = 0$) and models with a cusp ($\gamma = 0.05$).

The inferred intrinsic anisotropy profile, distance, and stellar mass-to-light ratio are all insensitive to the exact light and mass distributions near the center. We find that the anisotropy changes from slightly radial near the center to significantly tangential in the outer parts. The presence of velocity anisotropy is not surprising, given the long two-body relaxation time of ω Centauri and the existence of other evidence that the cluster is not yet fully relaxed. The inferred distance is 4.73 ± 0.09 kpc and the mass-to-light ratio is $\Upsilon_V = 2.62 \pm 0.06$. The error bars take into account both the uncertainties in the kinematical data and the uncertainty in the cusp slope γ. These results match extremely well with those obtained by vdV06 using more sophisticated modeling tools. This agreement supports our assertion that spherical models based on the Jeans equation are sufficient for the goals of the present paper, and in particular for constraining the mass distribution near the center. The facts that the ellipticity and rotation of ω Centauri are both known to decrease towards the center provide further motivation for this assertion.

Models with a core provide a good fit to the kinematical data without any dark mass. Since a core is also consistent with the observed density profile, this implies that the presence of an IMBH is not required in ω Centauri. By contrast, models with a shallow cusp provide a good fit only when an IMBH is invoked, with $M_{\rm BH} = (8.7 \pm 2.9) \times 10^3\ M_\odot$. Indeed, an IMBH can induce a shallow density cusp (Baumgardt, Makino & Hut 2005). Without a dark mass, the predicted RMS velocities in the cusp model decrease towards the cluster center and the predicted velocity distributions become highly non-Gaussian. Neither prediction is consistent with the observations.

Upon combination of the predictions for the core and cusp models we obtain as final result an upper limit to the mass of any possible IMBH of $1.2 \times 10^4\ M_\odot$ at 1σ confidence (or $1.8 \times 10^4\ M_\odot$ at 3σ confidence). The 1σ limit corresponds to $M_{\rm BH}/M_{\rm tot} \lesssim 0.43\%$. This is of similar magnitude as the range that has now been probed for several other clusters as well. However, lower values of $M_{\rm BH}/M_{\rm tot}$ will need to be probed to definitively assess the most plausible theories for IMBH formation in globular clusters, or to assess whether globular clusters may follow the same black hole demographics correlations as galaxies.

Isotropic models are not accurate for ω Centauri, since they do not reproduce the observed deviations of $[\bar\Sigma_{\rm pmt}/\bar\Sigma_{\rm pmr}](R)$ from unity. Use of isotropic models to fit $\bar\sigma(R)$ yields spuriously high IMBH masses. Isotropic

models do provide a reasonable guide for calculation of predicted velocity distribution shapes (as opposed to RMS values) in the central region. The predicted Gauss-Hermite moments as function of radius for such models fit the observations in the central arcmin to within $|\Delta h_i| \lesssim 0.01$. In models with an IMBH, the wings of the velocity distribution for an aperture on the very center are predicted to be more extended than in models without an IMBH. However, for cusp models with plausible IMBH masses we would not have expected more than a single star in the data set to have a velocity component in excess of $60\,\mathrm{km\,s^{-1}}$ (~ 3.5 times the cluster velocity dispersion). No such stars were observed in our data. Given the small number statistics, this does not provide meaningful new constraints on the IMBH mass for this particular cluster.

The dark mass invoked in cusp models may in principle be extended. The χ^2 of the fit yields a limit $a_{\rm dark} \lesssim 7'' = 0.16$ pc on the extent of any dark cluster at 1σ confidence. The corresponding central density is $\gtrsim 500$ times larger than the central density of luminous matter. This would be indicative of quite an extreme amount of mass segregation. If ω Centauri does have a cusp and a dark mass, then an IMBH may be easier to explain theoretically than such a concentrated dark cluster.

The IMBH mass suggested by NGB08 is strongly ruled out in all models. They found $M_{\rm BH} = 4.0^{+0.75}_{-1.0} \times 10^4\,M_\odot$ from isotropic modeling and $M_{\rm BH} = (3.0 \pm 1.0) \times 10^4\,M_\odot$ from anisotropic modeling. By contrast, we find that any IMBH in excess of $1.8 \times 10^4\,M_\odot$ is ruled out at 3σ or higher confidence. This difference is not surprising, given that our observations have not reproduced the arguments on which their IMBH mass was based (namely, their choice of cluster center, their finding of an increase in dispersion towards that center, and their finding of a cusp around that center). If one ignores these fundamental differences, then maybe our results do not appear so different from those NGB08. When comparing similar models between the two studies (i.e., cusp models with and without anisotropy), the differences in the implied IMBH masses are at the $\sim 2\sigma$ confidence level, given the uncertainties quoted by NGB08 (with our masses being lower). However, the more important difference is that we find that core models with no IMBH are perfectly consistent with the data. By contrast, NGB08 concluded that models with a core and models without an IMBH were ruled out with least 3σ confidence. So while NGB08 argued for a significant IMBH detection, we find by contrast that there is no need to invoke an IMBH in Omega Cen at all. Our finding that ω Centauri cannot have an IMBH as massive as suggested by NGB08 is consistent with arguments presented by Maccarone & Servillat (2008). They found that accretion models with the NGB08 IMBH mass predict much more X-ray and radio emission than is observed from the cluster center.

To further strengthen the conclusions from this paper and our understanding of ω Centauri, it will be useful to proceed with the construction of more sophisticated equilibrium models. Methods for numerical creation of axisymmetric models through orbit superposition have been developed by, e.g., vdV06, van den Bosch et al. (2006), and Chaname et al. (2008). These models can fit the observed differences between major and minor axis kinematics (discussed in Appendix B). They can also make use of the 47,781 high-quality proper motions along the major axis at $R \approx 1$–6 arcmin, which were excluded from consideration here (discussed in Appendix C). This will yield constraints on the inclination, rotation properties, and the presence of any kinematic subcomponents. It should also yield further improved limits on the possible presence of any dark mass in the center. Construction of non-equilibrium models for ω Centauri would be useful as well. N-body, Monte-Carlo, or Fokker-Planck models might shed light on the evolutionary status of ω Centauri, and on how it arrived at its present structure. This would also provide a more self-consistent description of the joint effects of mass segregation and energy equipartition than we have provided here. Moreover, it would be able to explicitly account for the Brownian motion of a possible IMBH.

We are grateful to Ivan King, Dean McLaughlin, Pat Seitzer, and Glenn van de Ven for useful discussions and/or providing data in electronic format. Suggestions from the referees helped us improve the presentation of our results.

APPENDIX

A. EXTRACTING KINEMATICS FROM DISCRETE DATA

To extract kinematics from a set of discrete data points, we select the stars that fall in a given area on the sky (e.g., a circular aperture, annulus, polar wedge, or square aperture). For these stars we then select the measurements $w_i \pm \Delta w_i$ in a given coordinate direction (e.g., line of sight, proper motion radial, proper motion tangential, proper motion major, or proper motion minor). The w_i may be either velocities in km/s or proper motions in mas/yr. The goal is to determine the underlying distribution from which the measurements are drawn. We assume that this is a Gaussian with mean W and dispersion σ, and we set out to determine W and σ with their error bars. If the measurement errors Δw_i are all identical then the problem has straightforward analytical solutions. However, this is not generally the case, so that more complicated analysis is required (e.g., Appendix A of vdV06).

We start with a trial estimate of σ. Each measurement w_i is then drawn from a Gaussian with dispersion $d_i = (\Delta w_i^2 + \sigma^2)^{1/2}$. Hence, the velocity W and its error bar ΔW follow from straightforward weighted averaging

$$S_1 \equiv \sum_i 1/d_i^2, \qquad S_2 \equiv \sum_i w_i/d_i^2, \qquad W = S_2/S_1, \qquad \Delta W = S_1^{-1/2}. \tag{A1}$$

We then determine the value of σ which maximizes the likelihood

$$L(\sigma) = \prod_i (2\pi\sigma^2)^{-1/2} \exp\{-(w_i - W)^2/(2[\Delta w_i^2 + \sigma^2])\}, \tag{A2}$$

by numerically solving the equation $dL/d\sigma = 0$. Having obtained σ, we return to an improved determination of W and we iterate the procedure until convergence. This provides a fixed point iteration scheme for determination of the joint maximum likelihood solutions for W and σ.

As described in Appendix A of vdV06, the maximum likelihood solution for σ yields a subtly biased estimate of the true dispersion. vdV06 used an analytical approximation to correct for this. Here we have used a Monte-Carlo procedure instead. After the determination of (W, σ), we draw pseudo-data sets from the corresponding Gaussian probability distribution. To this we add random Gaussian errors drawn from the observational uncertainties. We then analyze numerous such pseudo-datasets in the same fashion as the real data. The statistics of the Monte-Carlo results provide both an estimate of the bias in σ (which we use to correct our maximum likelihood estimate) and of the uncertainty $\Delta\sigma$.

After the calculation of W and σ has been completed, the RMS value $\bar{\sigma}$ and its uncertainty can be obtained from

$$\bar{\sigma} = (W^2 + \sigma^2)^{1/2}, \qquad \Delta\bar{\sigma} = [(W\,\Delta W)^2 + (\sigma\,\Delta\sigma)^2]^{1/2}/\bar{\sigma}. \tag{A3}$$

For the HST proper motion data, our analysis procedure removed all mean motions (see Section 5.2.3). Therefore, we know that the mean of the underlying distribution for any data set extracted from it should be $W = 0$. For this case we determined $\bar{\sigma}$ more efficiently as the solution of the maximum likelihood equation $dL/d\sigma = 0$ at fixed $W \equiv 0$.

B. MAJOR VERSUS MINOR AXIS

In a spherical system one expects the projected kinematics to be the same along any axis through the center. One also expects that the projected kinematics for the proper motion coordinate along any fixed direction, when averaged over a circle, will be independent of the chosen direction. These expectations are not realized in practice, and this provides a kinematical signature of the axisymmetry of ω Centauri. vdV06 discussed this in detail for the ground-based kinematical data. Here we briefly discuss this issue for the HST proper motion data.

We have extracted major and minor axis subsamples from our HST proper motion sample, consisting of the stars lying within 10° from either axis. When averaged over all radii $R \leq 71.7''$, we find for the radial proper motion direction that $\bar{\Sigma}_{\rm pmr} = 0.758 \pm 0.010\,{\rm mas\,yr^{-1}}$ along the major axis, and $\bar{\Sigma}_{\rm pmr} = 0.739 \pm 0.010\,{\rm mas\,yr^{-1}}$ along the minor axis. For the tangential proper motion direction we find that $\bar{\Sigma}_{\rm pmt} = 0.691 \pm 0.009\,{\rm mas\,yr^{-1}}$ along the major axis, and $\bar{\Sigma}_{\rm pmt} = 0.764 \pm 0.010\,{\rm mas\,yr^{-1}}$ along the minor axis. In a spherical system the kinematics would be the same along the two axes. In reality, $\bar{\Sigma}_{\rm pmr}$ is $(2.5 \pm 1.8)\%$ lower along the minor axis than along the major axis, while $\bar{\Sigma}_{\rm pmt}$ is $(10.6 \pm 2.1)\%$ higher along the minor axis than along the major axis. There is no statistically significant variation with radius in these comparisons (for $R \leq 71.7''$).

An alternative way to look at these results is to consider the fixed major and minor directions on the sky, and to measure the RMS projected proper motion components $\bar{\Sigma}_{\rm pmmj}$ and $\bar{\Sigma}_{\rm pmmi}$ along these directions, respectively. For the major axis subsample we find $\bar{\Sigma}_{\rm pmmj}/\bar{\Sigma}_{\rm pmmi} \approx \bar{\Sigma}_{\rm pmr}/\bar{\Sigma}_{\rm pmt} = 1.097 \pm 0.021$. For the minor axis subsample we find $\bar{\Sigma}_{\rm pmmj}/\bar{\Sigma}_{\rm pmmi} \approx \bar{\Sigma}_{\rm pmt}/\bar{\Sigma}_{\rm pmr} = 1.039 \pm 0.020$. When averaged over the whole sample (i.e., over all position angles) we find that $\bar{\Sigma}_{\rm pmmj}/\bar{\Sigma}_{\rm pmmi} = 1.048 \pm 0.007$. Therefore, the RMS projected velocity along the major axis is always larger than that along the minor axis. This was also found by vdV06, who obtained for the 718 stars with all three velocity components measured that $\bar{\Sigma}_{\rm pmmj}/\bar{\Sigma}_{\rm pmmi} = 1.055 \pm 0.053$ (see their Appendix C and also their Figure C.1).

These results are relatively easily understood heuristically. For an axisymmetric system that is not too far from edge-on, $\bar{\Sigma}_{\rm pmmj}$ is primarily related to the pressure along the equatorial plane and $\bar{\Sigma}_{\rm pmmi}$ is primarily related to the pressure along the symmetry axis. The former must exceed the latter in an oblate system, as dictated by the tensor virial theorem (e.g., Binney & Tremaine 1987).

C. PROPER MOTION KINEMATICS FOR THE MAJOR AXIS HST FIELD

As discussed in Section 5.2.1, there is also proper motion data available from Paper I for another field that was observed at multiple epochs with HST. This field lies roughly along the major axis, and therefore does not provide coverage of the full range of position angles in ω Centauri. We therefore did not use it for our model fitting. However, we address here the major axis profiles that can be extracted from these data. This allows a comparison with the central field and our model predictions to check for consistency.

We defined both for the central field and the major axis field a major-axis subsample consisting of stars lying within 10° from the major axis. This is the largest wedge for which coverage over the full range of allowed position angles is guaranteed at the majority of radii R. For the central field we have complete coverage for $R \leq 115''$. For the major axis field we have complete coverage for $108'' \leq R \leq 292''$. We extracted the profiles of $\bar{\Sigma}_{\rm pmr}(R)$ and $\bar{\Sigma}_{\rm pmt}(R)$ for both subsamples, following the procedures described in Section 5.2.2. The results are shown in Figure 11. The HST profiles are continuous at the boundary between the central and major axis fields, as they should be.

At radii $R \leq 71.7''$, we have complete coverage in the central field over all position angles. We can therefore calculate the ratios of the projected RMS proper motions measured within 10° from the major axis and averaged over an entire circle, respectively. This yields $(\bar{\Sigma}_{\rm pmr})_{\rm maj}/(\bar{\Sigma}_{\rm pmr})_{\rm circ} = 1.011 \pm 0.014$ and $(\bar{\Sigma}_{\rm pmt})_{\rm maj}/(\bar{\Sigma}_{\rm pmt})_{\rm circ} = 0.938 \pm 0.014$. If we assume as a simple approximation that these ratios are independent of radius, then this allows us to compare the predictions of our dynamical models to the observed major axis profiles. The curves in Figure 11 are the model predictions for our best-fitting anisotropic model with a core and no dark mass (see Figure 7a), scaled by the previously quoted ratios $(\bar{\Sigma}_{\rm pmr})_{\rm maj}/(\bar{\Sigma}_{\rm pmr})_{\rm circ}$ and $(\bar{\Sigma}_{\rm pmt})_{\rm maj}/(\bar{\Sigma}_{\rm pmt})_{\rm circ}$.

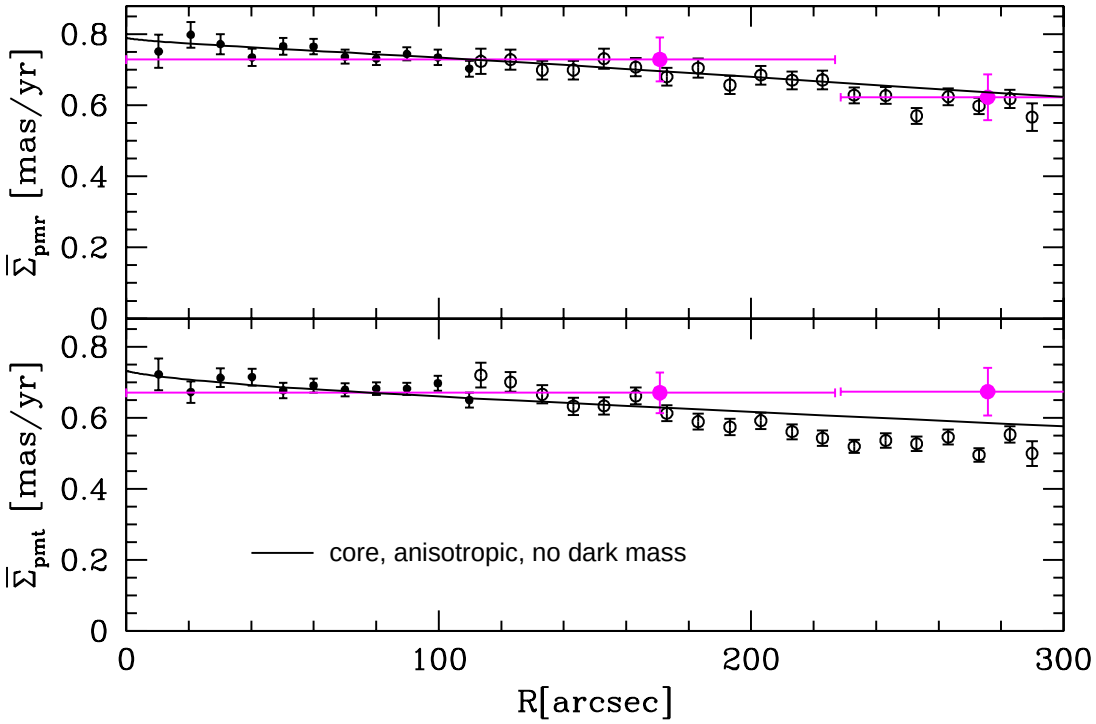

FIG. 11.— Observed major axis profiles of the RMS projected proper motions $\bar{\Sigma}_{\rm pmr}$ and $\bar{\Sigma}_{\rm pmt}$ in mas/yr, as function of projected radius R from the cluster center. Symbols are the same as in Figure 3b. For the HST data points we included stars within 10° from the major axis. For the vdV06 data points (magenta in the on-line version, with horizontal error bars) we included stars within a slightly larger angle from the major axis (17.5°), to increase the sample size. The vdV06 motions were multiplied by a factor 1.023 to correct to the same characteristic main-sequence stellar mass as for the HST sample (see Section 5.1.3). HST data points at $R < 110''$ (closed dots) are based on the data from the central field, and those at $R > 110''$ (open dots) are based on the major axis field. The figure focuses on the central region and uses a linear scale in R, by contrast to Figure 3b. The curves are predictions based on the best-fitting anisotropic model with a core and no dark mass, as discussed in the text. The data for the major axis field are consistent with expectation, given the detailed modeling of the central field and the inability of the HST data to measure absolute rotation in the pmt direction.

The model curves thus obtained provide an excellent fit to the $\bar{\Sigma}_{\rm pmr}(R)$ data for the major axis field. Also, the $\bar{\Sigma}_{\rm pmr}(R)$ data for the major axis field are consistent with the data from vdV06, which are also shown in the figure. By contrast, the fit to the $\bar{\Sigma}_{\rm pmt}(R)$ data for the major axis field is good only for $R \lesssim 200''$. At larger radii, the data fall below the model, and they also fall below the data from vdV06. We attribute this to the inability of the HST proper motion data to measure absolute rotation $\mathcal{V}_{\rm pmt}$. As a result, we expect to progressively underestimate $\bar{\Sigma}_{\rm pmt}$ with increasing radius, since $\mathcal{V}_{\rm pmt}/\Sigma_{\rm pmt}$ increases with radius (see Section 5.2.3). The fact that the data-model comparison is more successful for $\bar{\Sigma}_{\rm pmr}(R)$ is explained by the fact that pmr is orthogonal to direction of absolute rotation, and it is therefore insensitive to it.

Taking into consideration the limitations inherent to the data for the major axis field, and the results presented here, we have no reason to believe that detailed modeling of the data for the major axis field would significantly alter the conclusions of our paper.

REFERENCES

Anderson, J. 2002, in Omega Centauri, A Unique Window into Astrophysics. ASP Conf. Proceedings, Vol. 265. F. van Leeuwen, J. D. Hughes, & G. Piotto, eds., p. 87 (San Francisco: Astronomical Society of the Pacific)

Anderson, J, & van der Marel, R. P. 2009, ApJ, submitted (Paper I)

Ardi, E., Baumgardt, H., & Mineshige, S. 2008, ApJ, 682, 1195

Bacon, R., Simien, F., & Monnet, G. 1983, A&A, 128, 405

Bahcall, J. N., & Wolf, R. A. 1976, ApJ, 209, 214

Bash, F. N., Gebhardt, K., Goss, W. M., & Vanden Bout, P. A. 2008, AJ, 135, 182

Baumgardt, H., Hut, P., Makino, J., McMillan, S., & Portegies Zwart, S. 2003, ApJ, 582, L21

Baumgardt, H., Makino, J., Hut, P., McMillan, S., & Portegies Zwart, S. 2003, ApJ, 589, L25

Baumgardt, H., Makino, J., & Hut, P. 2005, ApJ, 620, 238

Binney, J. J., & Mamon, G. A. 1982, MNRAS, 200, 361

Binney, J. J., & Merrifield, M. 1998, Galactic Astronomy (Princeton: Princeton University Press)

Binney J. J., & Tremaine S. 1987, Galactic Dynamics (Princeton: Princeton University Press)

Cappellari, M. et al. 2007, MNRAS, 379, 418

Chakrabarty, D. 2006, AJ, 131, 2561

Chaname, J., Kleyna, J., & van der Marel, R. P. 2008, ApJ, D

Chatterjee, P., Hernquist, L., & Loeb, A. 2002, ApJ, 572, 371

Cretton, N., de Zeeuw, P. T., van der Marel, R. P., & Rix, H.-W. 1999, ApJS, 124, 383

Da Costa, G. S. 1979, AJ, 84, 505

Dejonghe, H. 1987, MNRAS, 224, 13

Dull, J. D., Cohn, H. N., Lugger, P. M., Murphy, B. W., Seitzer, P. O., Callanan, P. J., Rutten, R. G. M., & Charles, P. A. 1997, ApJ, 481, 267 (see also addendum, 2003, ApJ, 585, 598)

Drukier, G. A., & Bailyn, C. D. 2003, ApJ, 597, L125

Freeman, K. C. 1993, in The globular clusters-galaxy connection. Astronomical Society of the Pacific Conf. Series, Vol. 48, G. H. Smith, J. P. Brodie, eds., p. 608 (San Francisco: Astronomical Society of the Pacific)

Freitag, M., Gurkan, M. A., & Rasio, F. A. 2006, MNRAS, 368, 141

Gascoigne, S. C. B., & Burr, E. J., 1956, MNRAS, 116, 570

Gebhardt, K., et al. 2000, AJ, 119, 1157

Gebhardt, K., & Fischer, P. 1995, AJ, 109, 209

Gebhardt, K., Rich, R. M., & Ho, L. C. 2002, ApJ, 578, L41

Gebhardt, K., Rich, R. M., & Ho, L. C. 2005, ApJ, 634, 1093

Gerhard, O. E. 1993, MNRAS, 265, 213
Gerssen, J., van der Marel, R. P., Gebhardt, K., Guhathakurta, P., Peterson, R., Pryor, C. 2002, AJ, 124, 3270 (addendum: 2003, AJ, 125, 376)
Geyer, E. H., Nelles, B., & Hopp, U. 1983, A&A, 125, 359
Gill, M., Trenti, M., Miller, M. C., van der Marel, R. P., Hamilton, D., & Stiavelli, M. 2008, ApJ, 686, 303
Gurkan, M. A., Freitag, M., & Rasio, F. A. 2004, 604, 632
Haering, N, & Rix, H.-W. 2004, 604, L89
Harris, W. E. 1996, AJ, 112, 1487
Ho, L. C., Terashima, Y., Okajima, T. 2003, ApJ, 587, L35
King, I. R. 1966, AJ, 71, 64
King, I. R., Hedemann, E. Jr., Hodge, S. M., & White, R. E. 1968, AJ, 73, 456
King, I., & Anderson, J. 2002, in Omega Centauri, A Unique Window into Astrophysics. ASP Conf. Proceedings, Vol. 265. F. van Leeuwen, J. D. Hughes, & G. Piotto, eds., p. 21 (San Francisco: Astronomical Society of the Pacific)
Kong, A. K. H. 2007, ApJ, 661, 875
Lauer, T. R., et al. 1995, AJ, 110, 2622
Leonard, P. J. T., & Merritt, D. 1989, ApJ, 339, 195
Maccarone, T. J., & Servillat, M. 2008, MNRAS, 389, 379
Mayor, M., et al. 1997, AJ, 114, 1087
McLaughlin, D. E., & Meylan, G. 2003, in New Horizons in Globular Cluster Astronomy, ASP Conf. Proc. 296, G. Piotto, G. Meylan, S. G. Djorgovski, M. Riello, eds., 153
McLaughlin, D. E., & van der Marel, R. P. 2005, ApJS, 161, 304
McLaughlin, D. E., Anderson, J., Meylan, G., Gebhardt, K., Pryor, C., Minniti, D., & Phinney, S. 2006, ApJS, 166, 249
McNamara, B. J., Harrison, T. E., & Anderson, J. 2003, ApJ, 595, 187
Merritt, D., Meylan, G., Mayor, M. 1997, AJ, 114, 1074
Merritt, D., Berczik, P., & Laun, F. 2007, AJ, 133, 533
Meylan, G., Sarajedini, A., Jablonka, P., Djorgovski, S. G., Bridges, T., & Rich, R. M. 2001, AJ, 122, 830
Meylan, G. 2002, in Omega Centauri, A Unique Window into Astrophysics. ASP Conf. Proceedings, Vol. 265. F. van Leeuwen, J. D. Hughes, & G. Piotto, eds., p. 3 (San Francisco: Astronomical Society of the Pacific)
Miller, M. C., & Colbert, E. J. M. 2004, International Journal of Modern Physics D, 13, 1
Noyola, E., Gebhardt, K., Bergmann, M. 2008, ApJ, 676, 1008 (NGB08)
O'Leary, R. M., Rasio, F. A., Fregau, J. M., Ivanova, N., & O'Shaughnessy, R. 2006, ApJ, 637, 937
Pancino, E., Galfo, A., Ferraro, F. R., & Bellazzini, M. 2007, ApJ, 661, L155
Pasquato, M., Trenti, M., De Marchi, G., Gill, M., Hamilton, D. P., Miller, M. C., Stiavelli, M., & van der Marel, R. P. 2009, ApJ, in press [arXiv:0904.3326]
Pooley, D., & Rappaport, S. 2006, ApJ, 644, L45
Portegies Zwart, S. F., & McMillan, S. L. W. 2002, ApJ, 576, 899
Press, W. H., Teukolsky, S. A., Vetterling, W. T., & Flannery, B. P. 1992, Numerical Recipes in FORTRAN (2d ed.; Cambridge: Cambridge Univ. Press)
Reijns, R. A., et al. 2005, A&A, 445, 503
Scarpa, R., Marconi, G., & Gilmozzi, R. 2003, A&A, 405, L15
Seitzer, P. O. 1983, Ph.D. thesis, Univ. Virginia
Seth, A., Agueros, M., Lee, D., & Basu-Zych, A. 2008, ApJ, 678, 116
Sollima, A., Bellazzini, M., Smart, R. L., Correnti, M., Pancino, E., Ferraro, F. R., & Romano, D. 2009, MNRAS, in press [arXiv:0904.0571]
Suntzeff, N. B., & Kraft, R. P. 1996, AJ, 111, 1913
Thomas, J., Saglia, R. P., Bender, R., Thomas, D., Gebhardt, K., Magorrian, J., & Richstone, D. 2004, MNRAS, 353, 391
Trager, S. C., King, I. R., & Djorgovski, S. 1995, AJ, 109, 218
Tremaine, S., Richstone, D. O., Byun, Y.-I., Dressler, A., Faber, S. M., Grillmair, C., Kormendy, K., & Lauer, T. 1994, AJ, 107, 634
Tremaine, S., et al. 2002, ApJ, 574, 740
Ulvestad, J. S., Greene, J. E., & Ho, L. C. 2007, ApJ, 661, L151
Valluri, M., Merritt, D., & Emsellem, E. 2004, ApJ, 602, 66
van de Ven, G., van den Bosch, R.C.E., Verolme, E.K., & de Zeeuw, P.T. 2006, A&A, 445, 513 (vdV06)
van den Bosch, R., de Zeeuw, T., Gebhardt, K., Noyola, E., & van de Ven, G. 2006, ApJ, 641, 852
van den Bosch, R., van de Ven, G., Verolme, E. K., Cappellari, M., & de Zeeuw, P. T. 2008, MNRAS, 385, 647
van Leeuwen, F., Le Poole, R. S., Reijns, R. A., Freeman, K. C., & de Zeeuw, P. T. 2000, A&A, 360, 472
van der Marel, R. P. 1994a, MNRAS, 270, 271
van der Marel, R. P. 1994b, ApJ, 432, L91
van der Marel, R. P. 2004, in Coevolution of Black Holes and Galaxies, L. C. Ho, ed., p. 37 (Cambridge: Cambridge University Press)
van der Marel, R.P., Cretton, N., de Zeeuw, P.T., & Rix, H.-W. 1998, ApJ, 493, 613
van der Marel, R. P., & Franx, M. 1993, ApJ, 407, 525
van der Marel, R. P., Gerssen, J., Guhathakurta, P., Peterson, R. C., & Gebhardt, K. 2002, AJ, 124, 3255
van der Marel, R. P., Magorrian, J., Carlberg, R. G., Yee, H. K. C., & Ellingson, E. 2000, AJ, 119, 2038
Walcher, C. J., et al. 2005, ApJ, 618, 237
Wilson, C. P. 1975, AJ, 80, 175
Wybo, M., & Dejonghe, H. 1995, A&A, 295, 347